Table 1. Absorbance and Fluorescence Properties of ZnAFs at pH 7.4[a]

Dye	free λ_{max}	ϵ[b]	Φ[c]	+Zn^{2+} λ_{max}	ϵ[b]	Φ[c]
ZnAF-2	490	7.8×10^4	0.023	492	7.6×10^4	0.3 2
ZnAF-2M	490	5.3×10^4	0.034	492	5.2×10^4	0.2 7
ZnAF-2MM	490	1.1×10^5	0.006	493	8.8×10^4	0.1 0
ZnAF-3	490	7.1×10^4	0.029	493	6.2×10^4	0.3 8
ZnAF-4	490	6.8×10^4	0.012	492	6.4×10^4	0.2 2
ZnAF-5	490	6.4×10^4	0.004	492	4.3×10^4	0.2 1

[a] All data were measured in 100 mM HEPES buffer (pH 7.4, $I = 0.1$ ($NaNO_3$)). [b] ϵ stands for extinction coefficient (M^{-1} cm^{-1}) measured at each λ_{max}. [c] Φ stands for quantum yield of fluorescence, determined using that of fluorescein (0.85) in 0.1 M NaOH aq. as a standard.

Table 2. Apparent Dissociation Constants (K_d) and Association and Dissociation Rate Constants (k_{on} and k_{off}) of ZnAFs in 100 mM HEPES Buffer (pH 7.4, $I = 0.1$ ($NaNO_3$)) at 25 °C

dye	K_d (M)	k_{on} ($M^{-1}s^{-1}$)	k_{off} (s^{-1})
ZnAF-2	2.7×10^{-9}	3.1×10^6	8.4×10^{-3}
ZnAF-2M	3.8×10^{-8}	1.3×10^6	4.9×10^{-2}
ZnAF-2MM	3.9×10^{-6}	6.9×10^4	0.28
ZnAF-3	7.9×10^{-7}	1.4×10^6	1.1
ZnAF-4	2.5×10^{-5}	1.6×10^6	51
ZnAF-5	6.0×10^{-4}	6.7×10^4	40

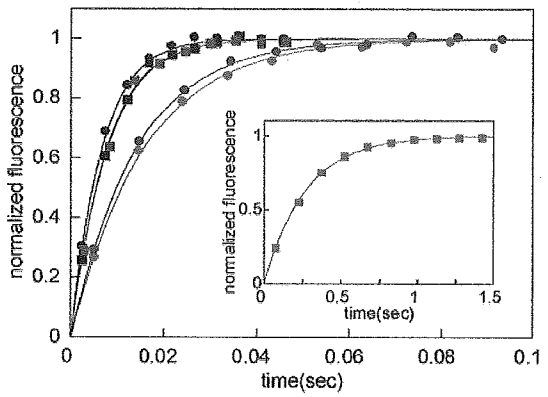

Figure 3. Time course measurement of the fluorescence intensity for 1 μM ZnAFs after mixing with Zn^{2+}. 50 μM Zn^{2+} was mixed with ZnAF-2 (black circle), ZnAF-2M (red circle), ZnAF-2MM (red square), and ZnAF-3 (blue circle). 1 mM Zn^{2+} was mixed with ZnAF-4 (black square) and ZnAF-5 (blue square). These data were measured in 100 mM HEPES buffer (pH 7.4, $I = 0.1$ ($NaNO_3$)) and 25 °C.

ZnAF-2, they show no response to biologically important metal ions, such as Ca^{2+} and Mg^{2+}, at millimolar concentration. Thus, the sensors with lower affinity for Zn^{2+} do not show reduced selectivity for Zn^{2+}. All the sensors have the same coordination atoms, and we think that this metal ion selectivity is mainly due to the character of nitrogen atom on the pyridine ring. In hard and soft acids and bases (HSAB) theory, pyridine is classified as a borderline base. It prefers Zn^{2+} to Ca^{2+} or Mg^{2+}, which is a hard acid. This preference would be important for the determination of the metal ion selectivity of ZnAFs. Some sensors show an increase in fluorescence intensity in the presence of some transition metals other than Zn^{2+}. Above all, Cd^{2+} shows a similar response to Zn^{2+}. However Cd^{2+} is rarely present in biological systems, so there would be no difficulty in biological applications.

Effect of pH. In addition to metal ion selectivity, it is important for many biological applications that the sensor does not respond to changes in pH. We measured the fluorescence intensity of ZnAFs at various pH values (Supporting Information, Figure S7). As in the case of ZnAF-2, the free bases of these sensors exhibit no significant emission enhancement upon acidification. Thus, the basal fluorescence intensity should be little affected by physiological pH changes.

Measuring Intracellular Zn^{2+}. We applied these sensor molecules to cultured cells or hippocampal slices. First, we measured the intracellular Zn^{2+} concentration of CHO cells to show their utility in fluorescence microscopic imaging by using membrane-permeable acetyl ester derivatives of ZnAF, ZnAF-2 DA,[19] and ZnAF-3 DA. These nonpolar compounds can easily penetrate through the cell membrane into the cytosol, where the acetyl groups are hydrolyzed by esterase to afford the Zn^{2+} sensors. After incubation with 10 μM sensors, cells showed weak fluorescence, suggesting that these sensors can be used intracellularly (data not shown). Then, we examined whether the difference of affinity is reflected in the fluorescence microscopic imaging of intracellular Zn^{2+} or not. The intracellular concentration of Zn^{2+} was controlled with a Zn^{2+} ionophore, pyrithione (2-mercaptopyridine *N*-oxide), which brings extracellular Zn^{2+} into the cytoplasm. We added various concentrations of Zn^{2+} with pyrithione, and the intracellular Zn^{2+} concentration was measured by fluorescence microscopy. Figure 5 shows the fluorescence response of each sensor molecule. With the increase of extracellular Zn^{2+} concentration from 0.3 to 300 μM, the fluorescence intensity of ZnAF-2 ($K_d = 2.7$ nM) was soon saturated. On the other hand, that of ZnAF-3 ($K_d = 0.79$ μM) was not saturated until 300 μM Zn^{2+}. This different response was clearly derived from the different affinity of the two sensors for Zn^{2+}. ZnAF-2 is superior for detecting lower Zn^{2+} concentrations, while ZnAF-3 can measure higher Zn^{2+} concentrations, which shows the importance of affinity for Zn^{2+} in cellular imaging. Thus, we can trace intracellular Zn^{2+} accurately by using combinations of several sensor molecules.

These results are in contrast with a previous report,[27] in which affinity for Zn^{2+} was suggested to be of less importance than dye concentration in fluorescence imaging; i.e., the dye concentration dominates the sensitivity of the reporting system. If the dye concentration is relatively high compared with the total ion pool available, the calibration of the dye signal to ion concentration may be affected, so care is necessary when using high intracellular dye concentrations. However, we consider that affinity is always an important factor in fluorescence imaging, as we have shown here. Using Zn^{2+} sensor molecules with suitable affinities should allow better calibration of the fluorescent signal to Zn^{2+} concentration.

(27) Dineley, K. E.; Malaiyandi, L. M.; Reynolds, I. J. *Mol. Pharmacol.* **2002**, *62*, 618–627.

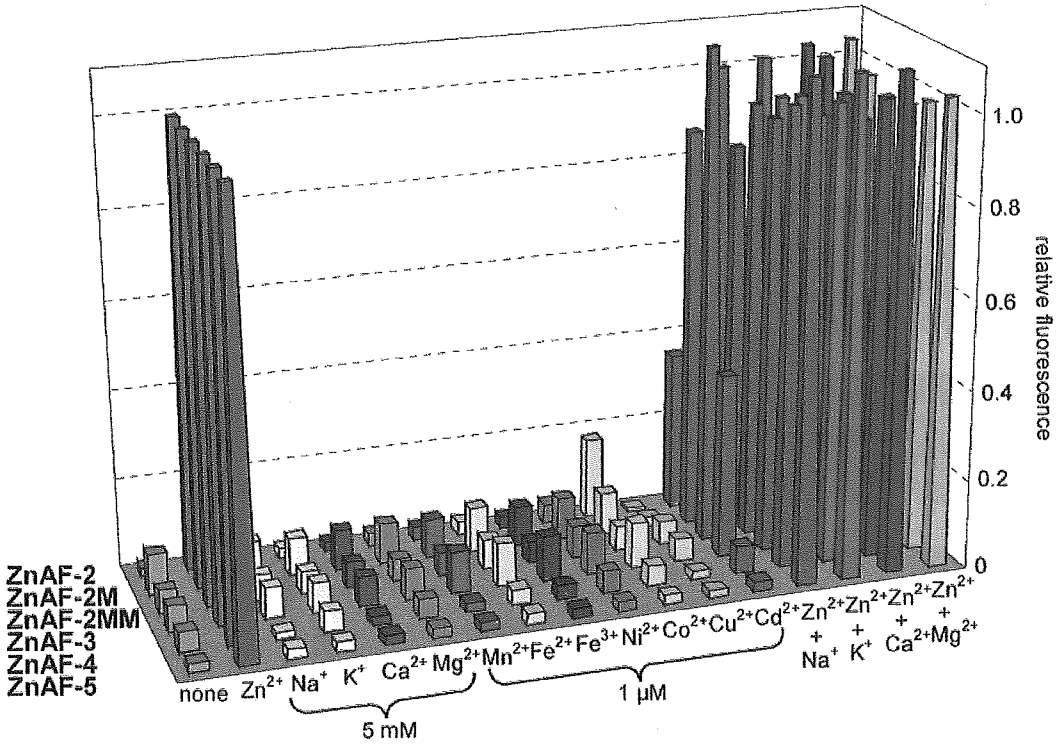

Figure 4. Relative fluorescence intensity of 1 μM ZnAFs in the presence of various metal ions. Na^+, K^+, Ca^{2+}, and Mg^{2+} were added at the concentration of 5 mM. Zn^{2+} was added at either 1 μM (ZnAF-2, ZnAF-2M) or 10 μM (ZnAF-2MM, ZnAF-3) or 100 μM (ZnAF-4, ZnAF-5). Other metals were added at 1 μM. These data were measured in 100 mM HEPES buffer (pH 7.4, I = 0.1 ($NaNO_3$)).

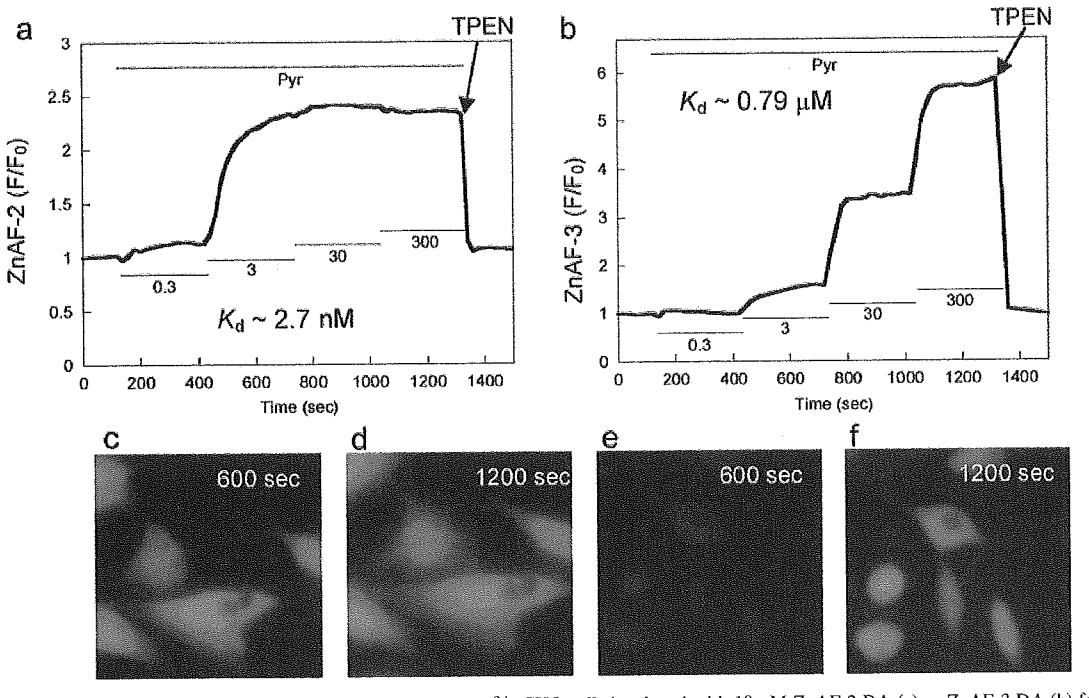

Figure 5. Fluorescence response of ZnAFs induced by intracellular Zn^{2+}. CHO cells incubated with 10 μM ZnAF-2 DA (a) or ZnAF-3 DA (b) for 30 min at room temperature were washed with PBS and fluorescence excited at 470−490 nm was measured at 20 s intervals. At 2 min, cells were exposed to pyrithione (Pyr, 100 μM) in the presence of sequentially increased concentrations of added extracellular Zn^{2+} (0.3, 3, 30, and 300 μM, each for 5 min) as indicated by the solid lines. Return of intracellular Zn^{2+} to the resting level was achieved by addition of TPEN (50 μM; starting at arrow). Fluorescence images incubated with ZnAF-2 DA (c, 600 s), (d, 1200 s), or ZnAF-3 DA (e, 600 s; f, 1200 s) are shown in the bottom panels.

Measuring Synaptically Released Zn^{2+}. For the analysis of Zn^{2+} in the central nervous system, we applied these sensors to hippocampal slices and measured synaptically released Zn^{2+} induced by membrane potential-depolarizing stimulation. All

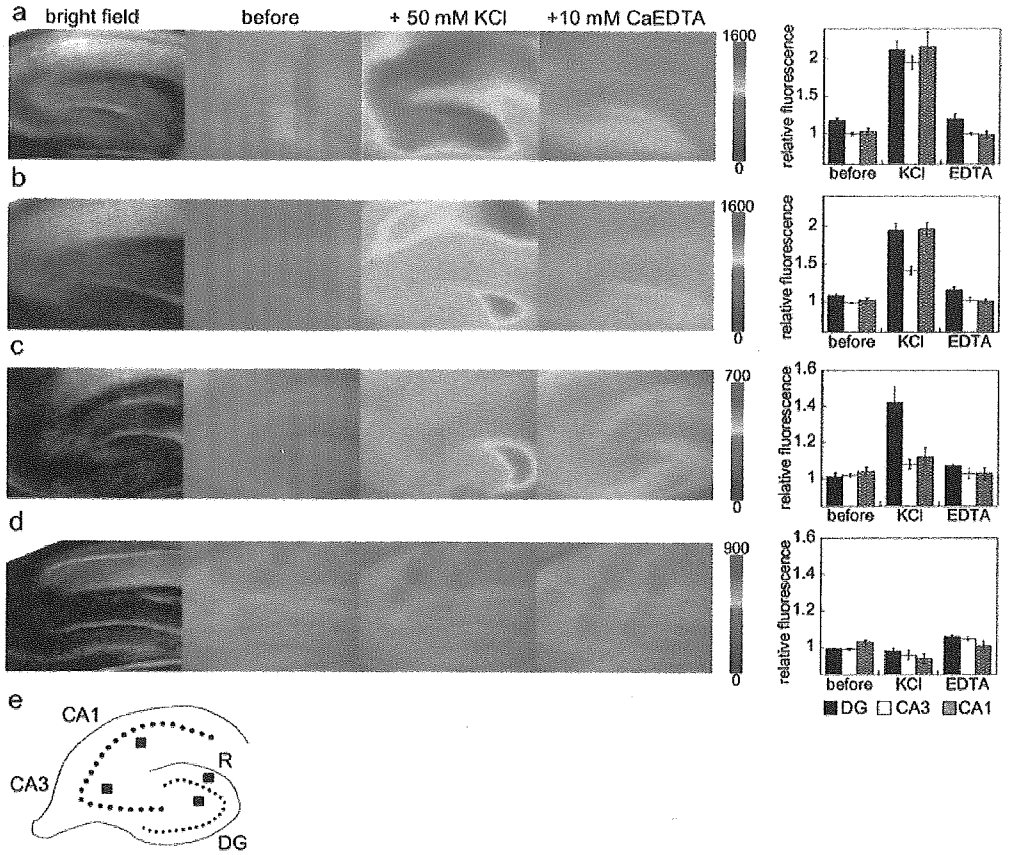

Figure 6. Fluorescence response of ZnAFs detecting extracellularly released Zn^{2+} in hippocampal slices. Fluorescence excited at 470−490 nm was measured soon after rat hippocampal slices were loaded with 1 μM ZnAF-2 (a), ZnAF-2M (b), ZnAF-3 (c), or ZnAF-4 (d). Then, 50 mM KCl (at 1 min) and 10 mM CaEDTA (at 10 min) were added to the imaging solution. Bright field images, fluorescence images at 0 min (before), at 3 min (+50 mM KCl), and at 15 min (+10 mM CaEDTA) are shown in each row. Relative fluorescence intensities of DG, CA3, and CA1 are shown in the bar graph, expressed as mean ± SE (n = 3 for ZnAF-2, ZnAF-3, and ZnAF-4 and n = 5 for ZnAF-2M). The bottom schematic (e) shows the approximate positions used for measurements of fluorescence intensity in the dentate gyrus (DG), CA3, CA1, and R (as a reference) region.

of the nerve terminals were stimulated into depolarization after addition of potassium ions. We observed a large fluorescence increase upon addition of 50 mM KCl to slices loaded with 1 μM ZnAF. To confirm that this fluorescence increase was due to an increase of extracellular Zn^{2+} concentration, we further added CaEDTA, an extracellular Zn^{2+} chelator. This treatment reduced the fluorescence intensity of ZnAF to the initial level, which confirmed that the indicator was responding to extracellular Zn^{2+} and that the extracellular Zn^{2+} concentration was below the detection level prior to depolarization. We acquired different fluorescence images after stimulation depending on the K_d value of the ZnAFs (Figure 6a−d). In the fluorescence imaging using ZnAF-2 (K_d = 2.7 nM), the fluorescence intensity increased mainly in three regions, the dentate gyrus (DG), CA3, and CA1, which were indistinguishable. Therefore, no regional difference of released Zn^{2+} concentration was observed using ZnAF-2, probably because of its high affinity for Zn^{2+}. With ZnAF-2M (K_d = 38 nM), on the other hand, the fluorescence intensity increased in DG and CA1, but increased less in CA3, and with ZnAF-3 (K_d = 0.79 μM), a fluorescence increase was seen only in DG. The lower affinity sensor, ZnAF-4 (K_d = 25 μM) showed no fluorescence increase. The mean increase of fluorescence intensity in each region is shown in the bar graph. So, these results demonstrate for the first time that a higher concentration of Zn^{2+} is released in DG than in CA3 or CA1, and a lower concentration of Zn^{2+} is released in CA3 than in DG or CA1.

A key advantage of using plural sensors is that estimation of the released Zn^{2+} concentration level is possible. In DG, there is a fluorescence response of ZnAF-3 (K_d = 0.79 μM) and no response of ZnAF-4 (K_d = 25 μM). Namely, the released Zn^{2+} concentration in DG is below the detection level for ZnAF-4. Thus, the released Zn^{2+} concentration is estimated to be of the order of 1 μM DG (Figure 2). Similarly, in both CA1 and CA3, there is a fluorescence response of ZnAF-2M (K_d = 38 nM) and no response of ZnAF-3. Thus, the released Zn^{2+} concentration level in CA1 and CA3 can be estimated to be of the order of 100 nM or less.

Thus, by using dyes with different affinity for Zn^{2+} for fluorescence imaging, we can obtain considerably more information from the same sample than would be possible with a single dye. Furthermore, it is clear that there is no single K_d value suitable for tracing all of the concentration levels of synaptically released Zn^{2+}, because a K_d value suitable for one region would give either no response or a saturated fluorescence signal in other regions. So, the importance of using several sensor molecules is clear, just as we had anticipated when designing this range of sensors. By virtue of having a spectrum

of affinities for Zn^{2+}, ZnAFs are the first Zn^{2+} sensor molecules not only to reveal regional differences but also to allow estimation of the concentrations of synaptically released Zn^{2+} in hippocampal slices. In addition, ZnAFs are also suitable for analyzing temporal changes of Zn^{2+}; a fast fluorescence increase and decrease in the CA1 region was visualized with ZnAF-2M (data not shown).

Previous reports indicate that electrical stimulation and potassium stimulation produce similar responses in terms of released Zn^{2+} concentration.[24] This would suggest that a similar concentration level of Zn^{2+} is released during natural neuronal activity. However, the reported concentration levels of released Zn^{2+} vary drastically. Li et al. suggested that synaptic release of Zn^{2+} during stimulation reaches micromolar levels.[24] They used the fluorescent sensor molecule Newport Green, which has an affinity of ~1 μM for Zn^{2+}. On the other hand, Kay examined synaptic release of Zn^{2+} using another fluorescent sensor molecule, FluoZin-3, whose K_d value is 15 nM and concluded that little Zn^{2+} (~6 nM) was released during stimulation.[28] Both estimations were done with a single sensor molecule, with quite different K_d values, and they utilized the maximum and minimum fluorescence intensity for Zn^{2+} calibration. However, our estimation is based on the use of several sensor molecules without relying on measurements of maximum or minimum fluorescence intensity. Moreover, our sensors have similar fluorescence properties, and only their affinity for Zn^{2+} differs. We think these features support the reliability of Zn^{2+} estimation with ZnAFs.

On the basis of the above results, our ZnAFs introduced here are expected to become useful tools in the investigation of Zn^{2+} biology, especially the role of Zn^{2+} in the central nervous system.[2d] These ZnAFs should have a wide range of application. In addition to synaptic release of Zn^{2+}, Zn^{2+} is suggested to be involved in excitotoxic neuronal death after head trauma, epilepsy, and cerebral ischemia and reperfusion.[29] Recently, extracellular accumulation of Zn^{2+} during ischemia and reperfusion was reported.[30] However, regional differences of Zn^{2+} over the areas of DG, CA3, and CA1 were not observed. Zn^{2+} sensor molecules with suitable K_d values may visualize regional differences, allowing detailed analysis of the Zn^{2+} distribution.

Although other Zn^{2+} sensor molecules with various affinities are available,[11g,13d] ZnAFs are the first sensor molecules suitable for both intra- and extracellular applications in biology. Combined with fluorescence microscopic imaging, ZnAFs have the potential to play a central role in the investigation of Zn^{2+} biology.

Conclusion

We have developed a range of fluorescent Zn^{2+} sensor molecules, ZnAF-2M, ZnAF-2MM, ZnAF-3, ZnAF-4, and ZnAF-5, whose K_d values range from nanomolar to subnanomolar levels. They all have similar fluorescence properties and differ only in their affinity for Zn^{2+}, without any loss of selectivity for Zn^{2+}. Using ZnAF-2 DA and ZnAF-3 DA, cell-permeable derivatives of ZnAFs, different responses to changes in intracellular Zn^{2+} concentration were observed. Extracellular Zn^{2+} release was also measured using ZnAFs and their use enabled us to detect regional difference in the Zn^{2+} release for the first time, as well as to estimate the approximate concentration of synaptically released Zn^{2+} in hippocampal slices. We can measure Zn^{2+} concentration over a wide range by using ZnAFs, which are expected to be useful probes for obtaining further insight into the physiological importance of Zn^{2+}.

Experimental Section

General Information. All reagents and solvents were of the highest commercial quality and were used without purification. ZnAF-2 and ZnAF-2 DA were purchased from Daiichi Pure Chemicals Co., Ltd. (Tokyo, Japan). ZnAF-2M, ZnAF-2MM, ZnAF-3, ZnAF-4, ZnAF-5, and ZnAF-3 DA were prepared as described in the Supporting Information. Dimethyl sulfoxide (DMSO), 2-[4-(2-hydroxyethyl)-1-piperazinyl]ethanesulfonic acid (HEPES), nitrilotriacetic acid (NTA), and *N,N,N′,N′*-tetrakis-(2-pyridylmethyl)ethylenediamine (TPEN) were purchased from Dojindo Laboratories, Ltd. (Kumamoto, Japan). All other reagents were purchased from either Tokyo Kasei Kogyo Co., Ltd. (Tokyo, Japan), or Wako Pure Chemical Industries, Ltd. (Osaka, Japan).

Fluorometric Analysis. Fluorescence spectroscopic studies were performed with a Hitachi F4500 (Tokyo, Japan). The slit width was 2.5 nm for both excitation and emission. The photomultiplier voltage was 750 V. ZnAFs were dissolved in DMSO to obtain 10 mM stock solutions. Fluorescence intensities of 1 μM ZnAFs as a function of free Zn^{2+} concentration were measured in 100 mM HEPES buffer (pH 7.4, $I = 0.1$ ($NaNO_3$)). Free Zn^{2+} concentration was controlled by using 0−9 mM $ZnSO_4$/10 mM NTA (nitrilotriacetic acid) systems[19a] for ZnAF-2 and ZnAF-2M and unbuffered Zn^{2+} for other ZnAFs. The fluorescence intensity data were fitted to eq 1, and K_d was calculated, where F is the fluorescence intensity, F_{max} is the maximum fluorescence intensity, F_0 is the fluorescence intensity with no addition of Zn^{2+}, and $[Zn^{2+}]_f$ is the free Zn^{2+} concentration.

$$F = F_0 + (F_{max} - F_0)([Zn^{2+}]_f)/(K_d + [Zn^{2+}]_f) \quad (1)$$

Relative quantum yields of fluorescence were obtained by comparing the area under the corrected emission spectrum of the sample at 492 nm with that of a solution of fluorescein in 0.1 M NaOH (quantum yield: 0.85). UV−visible spectra were measured with a Shimadzu UV-1600 (Tokyo, Japan).

Stopped-Flow Measurements. Stopped-flow experiments were performed with a SF-61 DX2 double-mixing stopped-flow spectrofluorimeter (Hi-Tech, Salisbury, U.K.) equipped with a monochromator between the 75 W xenon light source and the reaction cuvette excitation window. The quartz sample cuvette and syringes containing the reactants were maintained at 25 ± 0.1 °C by a circulating water bath. The pneumatic cylinder was driven by a nitrogen pressure of 6 bar, which resulted in an instrument dead time of 1 ms. A solution of 2 μM ZnAF in 100 mM HEPES buffer (pH 7.4, $I = 0.1$ ($NaNO_3$)) was combined with an equal volume of 100 μM or 2 mM of $ZnSO_4$. Fluorescence was measured with excitation at 492 nm and with emission at >530 nm, using a 530 cutoff filter. The fluorescence intensity data were fitted to eq 2, and k_{obs} was obtained, where F is the normalized fluorescence. Then, k_{on} and k_{off} were calculated as described previously.[19b]

$$F = 1 - \exp(-k_{obs}t) \quad (2)$$

Imaging System. The imaging system was comprised of an inverted fluorescence microscope (IX-71; Olympus, Tokyo, Japan), CoolSNAP HQ CCD camera (Roper Scientific, Tucson, AZ), and an image processor (MetaFluor; Universal Imaging Corp., Downingtown, PA). The microscope was equipped with a xenon lamp (AH2-RX; Olympus), an objective lens for CHO cells (PlanApo 60×/1.40 oil; Olympus) or

(28) Kay, A. R. *J. Neurosci.* **2003**, *23*, 6847−6855.
(29) (a) Choi, D. W.; Koh, J. Y. *Annu. Rev. Neurosci.* **1998**, *21*, 347−375. (b) Frederickson, C. J.; Hernandez, M. D.; McGinty, J. F. *Brain Res.* **1989**, *480*, 317−321. (c) Suh, S. W.; Chen, J. W.; Motamedi, M.; Bell, B.; Listiak, K.; Pons, N. F.; Danscher, G.; Frederickson, C. J. *Brain Res.* **2000**, *852*, 268−273.
(30) Wei, G.; Hough, C. J.; Li, Y.; Sarvey, J. M. *Neuroscience* **2004**, *125*, 867−877.

for hippocampal slices (UPlanAPo 4×/0.16; Olympus), an excitation filter (BP470-490; Olympus), a dichroic mirror (DM505; Olympus), and an emission filter (BA510-550; Olympus).

Preparation of Cells. CHO cells were cultured in Alpha medium (αMEM; Invitrogen Corp., Carlsbad, CA) containing 10% fetal bovine serum (Invitrogen Corp.), 1% penicillin (Invitrogen), and 1% streptomycin (Invitrogen) at 37 °C in a 5/95 CO_2/air incubator. Cells were passaged 3 days before dye loading on a 35 mm glass-based dish (Iwaki, Funabashi, Japan). Then the cells were rinsed with phosphate-buffered saline (PBS; Invitrogen), and incubated with PBS containing 10 μM ZnAF-2 DA or ZnAF-3 DA for 30 min at 37 °C. The cells were washed with PBS twice and mounted on the microscope stage. Fluorescence excited at 470−490 nm was measured at 20 s intervals, and the responses of three cells were compiled to generate a single trace.

Preparation of Rat Hippocampal Slices. The whole brains of adult Wistar rats (male, 200−250 g) were removed quickly under ether anesthesia and placed in ice-cold ACSF (artificial cerebrospinal fluid), which was aerated with 95/5 O_2/CO_2. The composition of ACSF was 124 mM NaCl, 2.5 mM KCl, 26 mM $NaHCO_3$, 1.25 mM NaH_2PO_4, 2.0 mM $CaCl_2$, 1.0 mM $MgCl_2$, and 10 mM glucose. The hippocampus was isolated, placed on an agar plate, and sliced into 300 μm thick slices with a rotary slicer (Model DTY 7700; Dosaka Co., Osaka, Japan). The fresh hippocampal slices were incubated in ACSF equilibrated with 95/5 O_2/CO_2 for more than 30 min at room temperature. Then each slice was transferred to a chamber on the microscope, where it was held in place by a metal wire ring with a stretched nylon net.

Acknowledgment. This work was supported in part by the Ministry of Education, Culture, Sports, Science and Technology of Japan (Grants for The Advanced and Innovational Research Program in Life Sciences to T.N., 15681012 and 16048206 to K.Kikuchi). K.Kikuchi was also supported by the Sankyo Foundation, by the Kanagawa Academy of Science, and by the Suzuken Memorial Foundation.

Supporting Information Available: Synthetic details and characterization of ZnAF-2M, ZnAF-2MM, ZnAF-3, ZnAF-4, ZnAF-5, and ZnAF-3 DA (PDF). This material is available free of charge via the Internet at http://pubs.acs.org.

JA050301E

THE JOURNAL OF BIOLOGICAL CHEMISTRY
Vol. 280, No. 22, Issue of June 3, pp. 21155–21161, 2005
Printed in U.S.A.

Inhibition of Autotaxin by Lysophosphatidic Acid and Sphingosine 1-Phosphate*[S]

Received for publication, November 22, 2004, and in revised form, February 18, 2005
Published, JBC Papers in Press, March 15, 2005, DOI 10.1074/jbc.M413183200

Laurens A. van Meeteren‡, Paula Ruurs‡, Evangelos Christodoulou§, James W. Goding¶, Hideo Takakusa‖, Kazuya Kikuchi‖, Anastassis Perrakis§, Tetsuo Nagano‖, and Wouter H. Moolenaar‡**

From the ‡Division of Cellular Biochemistry and Center for Biomedical Genetics and §Division of Molecular Carcinogenesis, The Netherlands Cancer Institute, Plesmanlaan 121, 1066 CX Amsterdam, The Netherlands, ¶Department of Pathology and Immunology, Monash Medical School, Alfred Hospital, Prahran 3181, Victoria, Australia, and ‖Graduate School of Pharmaceutical Sciences, University of Tokyo, Tokyo 113-0033, Japan

Autotaxin (ATX) or nucleotide pyrophosphatase/phosphodiesterase 2 (NPP2) is an NPP family member that promotes tumor cell motility, experimental metastasis, and angiogenesis. ATX primarily functions as a lysophospholipase D, generating the lipid mediator lysophosphatidic acid (LPA) from lysophosphatidylcholine. ATX uses a single catalytic site for the hydrolysis of both lipid and non-lipid phosphodiesters, but its regulation is not well understood. Using a new fluorescence resonance energy transfer-based phosphodiesterase sensor that reports ATX activity with high sensitivity, we show here that ATX is potently and specifically inhibited by LPA and sphingosine 1-phosphate (S1P) in a mixed-type manner ($K_i \sim 10^{-7}$ M). The homologous ecto-phosphodiesterase NPP1, which lacks lysophospholipase D activity, is insensitive to LPA and S1P. Our results suggest that, by repressing ATX activity, LPA can regulate its own biosynthesis in the extracellular environment, and they reveal a novel role for S1P as an inhibitor of ATX, in addition to its well established role as a receptor ligand.

Autotaxin (ATX)[1] is a member of the nucleotide pyrophosphatase/phosphodiesterase (NPP) family of ecto-enzymes that hydrolyze phosphodiester bonds in various nucleotides and nucleotide derivatives (1–3). ATX, also termed NPP2, was originally isolated as an autocrine motility factor for melanoma cells (4, 5) and later found to enhance the invasive and metastatic potential of Ras-transformed NIH3T3 cells in nude mice and to induce an angiogenic response in Matrigel plug assays (6, 7). ATX mRNA is overexpressed in various human cancers, adding support to a link between ATX and tumor progression (8). Expression analysis has further suggested a normal physiological role for ATX in neurogenesis, oligodendrocyte differentiation, and myelination (9, 10).

The mode of action of ATX/NPP2 has long been elusive because the biological effects of ATX could not be explained by nucleotide hydrolysis. The surprise came when it was discovered that ATX is identical to plasma lysophospholipase D (lyso-PLD) and acts by hydrolyzing lysophospatidylcholine (LPC) into lysophosphatidic acid (LPA) (11, 12), a lipid mediator that signals cell proliferation, migration, and survival via specific G protein-coupled receptors (13). It has now become clear that *de novo* production of LPA can fully account for the biological effects of ATX observed in cell culture. The lysophospholipid substrate range of ATX has recently been broadened by showing that the enzyme can also hydrolyze sphingosylphosphorylcholine (SPC) to yield sphingosine 1-phosphate (S1P) (14), a bioactive lipid with signaling properties very similar to those of LPA while acting on distinct receptors (15–17). The physiological significance of the SPC-to-S1P conversion is debatable, however, because the reported K_m of ATX for SPC (14) is 3 orders of magnitude higher than the normal SPC levels in plasma and serum (18). Rather than through SPC hydrolysis, S1P is thought to originate largely from the phosphorylation of sphingosine by sphingosine kinases (19).

Mutational analysis has revealed that the lyso-PLD and nucleotide phosphodiesterase activities of ATX originate from the same catalytic site (20, 21). Unexpectedly, the other two members of the NPP family (NPP1 and NPP3) lack intrinsic lyso-PLD activity despite their close homology to ATX (21). Given the differences in substrate specificity, it is not surprising that the NPPs appear to have largely unrelated physiological functions. The founding member, NPP1, hydrolyzes ATP into pyrophosphate, an inhibitor of calcification, and thereby regulates bone mineralization, whereas the third member, NPP3, promotes differentiation and invasion of glial cells by an unknown mechanism (3).

An unresolved question concerns the regulation of ATX activity. One puzzling observation is that LPA levels in plasma or freshly isolated blood are very low (22–24), yet plasma ATX is constitutively active and its substrate LPC abundantly present (> 100 μM) (25). This suggests that ATX is negatively regulated *in vivo*, but physiological or pharmacological inhibitors of ATX have not been identified to date. In the present study we sought to examine how ATX activity is regulated in the extracellular milieu. To this end, we used a newly invented fluorescence resonance energy transfer (FRET)-based phosphodiesterase sensor (termed CPF4; see Ref. 26) that, as we show here, reports ATX activity in conditioned media with superior sensitivity. Using this assay system, we demonstrate that ATX,

* This work was supported by the Dutch Cancer Society. The costs of publication of this article were defrayed in part by the payment of page charges. This article must therefore be hereby marked "*advertisement*" in accordance with 18 U.S.C. Section 1734 solely to indicate this fact.

[S] The on-line version of this article (available at http://www.jbc.org) contains supplemental Fig. 1.

** To whom correspondence should be addressed. Tel.: 31-20-512-1971; Fax: 31-20-512-1989; E-mail: w.moolenaar@nki.nl.

[1] The abbreviations used are: ATX, autotaxin; BSA, bovine serum albumin; FRET, fluorescence resonance energy transfer; LPA, lysophosphatidic acid; LPC, lysophosphatidylcholine; NPP, ectonucleotide pyrophosphatase/phosphodiesterase; PLD, phospholipase D; lyso-PLD, lysophospholipase D; SPC, sphingosylphosphorylcholine; S1P, sphingosine 1-phosphate; pNP, *para*-nitrophenolate; pNP-TMP, *para*-nitrophenyl thymidine-5′-monophosphate; bis-pNPP, bis(*para*-nitrotrophenyl) phosphate; GFP, green fluorescent protein; HA, hemagglutinin.

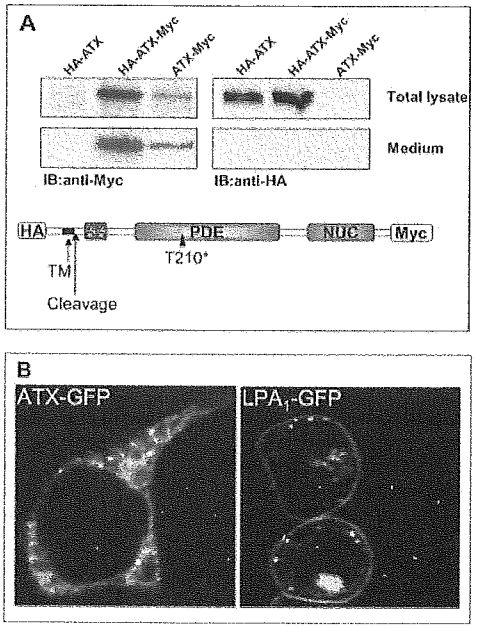

FIG. 1. **ATX processing and secretion.** *A*, human full-length ATX was expressed in HEK293T cells as a fusion protein with an N-terminal HA tag and/or a C-terminal Myc tag, as indicated. ATX expression in cell lysates and conditioned medium was analyzed by Western blotting using antibodies against the HA and Myc epitopes. Equal amounts of cell lysate and medium were applied in each experiment. HA-ATX is undetectable in the medium, consistent with N-terminal cleavage prior to secretion. *IB*, immunoblot; *TM*, transmembrane domain; *SO*, somatomedin-like domain; *PDE*, phosphodiesterase domain; *NUC*, nuclease-like domain. threonine residue (*T210*) is essential for catalytic activity. *B*, subcellular localization of ATX and the LPA_1 receptor (both C-terminally fused to GFP) in HEK293T cells. Unlike LPA_1, ATX is not detected at the cell surface but, instead, localizes to intracellular vesicles and reticular structures. Cells transfected with ATX-GFP or LPA_1-GFP (28) were fixed with ice-cold methanol at 24 h after transfection.

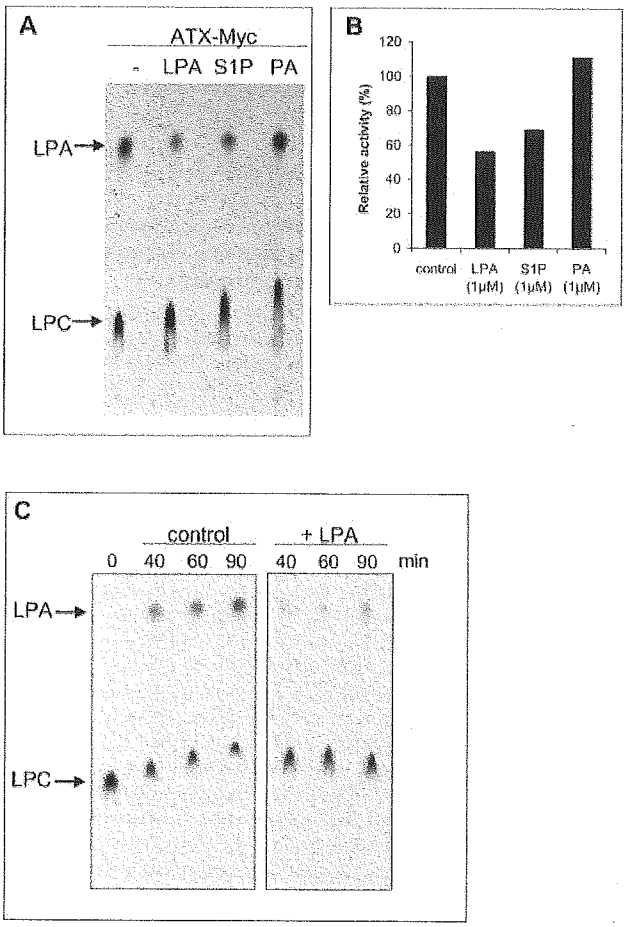

FIG. 2. **lyso-PLD activity of ATX.** *A*, lyso-PLD activity. Hydrolysis of 1-[1-^{14}C]palmitoyl-LPC into LPA by ATX-Myc in conditioned medium was analyzed by thin layer chromatography. The concentration of unlabeled LPC was 1 μM. The reaction was terminated after 2 h. LPC and LPA standards were run separately (not shown). LPA, S1P, and phosphatidic acid (*PA*) were added at 1 μM. *B*, graphical representation of data from two independent thin layer chromatography assays. *C*, time course of LPC hydrolysis into LPA and inhibition by LPA, added at 1 μM.

secreted by the classical export route, is potently and specifically inhibited by LPA and S1P at biologically relevant concentrations. These results have important implications for lysophospholipid action and signaling in general and ATX targeting in particular.

EXPERIMENTAL PROCEDURES

Cell Culture and Materials—HEK293T cells were grown in Dulbecco's modified Eagle's medium containing 10% fetal calf serum. All phospholipids were obtained from Avanti Polar Lipids Inc. (Alabaster, AL). Brefeldin A, monensin, BSA, fatty acid-free BSA (99%), *para*-nitrophenyl thymidine-5′-monophosphate (pNP-TMP), and bis(*para*-nitrotrophenyl) phosphate (bis-pNPP) were from Sigma. Highly purified PLD from *Streptomyces chromofuscus*, sphingomyelinase D from *Loxosceles laeta*, and sphingomyelinase D from *Corynebacterium pseudotuberculosis* were kindly provided by M. Roberts (Boston College), D. Tambourgi (Instituto Butantan, Sao Paulo, Brazil), and S. Billington (University of Arizona), respectively.

cDNA Cloning—RNA extracted from human diploid foreskin fibroblasts was used to generate cDNA using Invitrogen reverse transcriptase. ATX cDNA was isolated using ATX-specific primers. The stop codon was removed and KpnI and NotI restriction sites were introduced at the 5′ and 3′ sites, respectively. After digestion, ATX was ligated in pcDNA3 vector with 3′ Myc tag (ATX-Myc), 5′ HA tag (HA-ATX), or 5′ HA tag and 3′ Myc tag (HA-ATX-Myc), and in pEGFP-N3 (ATX-GFP). Sequencing showed that the ATX inserts were identical to human ATX (GenBank™ accession number BC034961). The catalytically inactive mutant ATX(T210A) (27) was generated using the Stratagene site-directed mutagenesis kit.

Transfection and Western Blotting—HEK293T cells were transfected with ATX constructs using the calcium phosphate method. At 24 h after transfection, cells were exposed to serum-free Dulbecco's modified Eagle's medium for 30 h. Conditioned medium was centrifuged (5000 rpm for 30 min) to remove cell debris. Medium was used without further purification and analyzed for the presence of ATX by Western blotting and activity assays. There was very little variation in ATX activity between different batches of conditioned medium. For Western blot analysis, nitrocellulose filters were blocked using 5% nonfat powdered milk and probed with primary antibodies (9E10 anti-Myc and 3F10 anti-HA; Roche Applied Science) and horseradish peroxidase-conjugated secondary antibodies (Dako, Glostrup, Denmark). Proteins were visualized using the ECL detection system (Amersham Biosciences).

Recombinant ATX—The Bac-to-Bac baculovirus expression system (Invitrogen) was used for ATX production. ATX cDNA fused to the honeybee melittin signal sequence at the 5′ end was cloned into the pFastBac I vector (Invitrogen). The resulting plasmid was then used for generating recombinant baculovirus to infect Sf9 insect cells, which were grown in SF-900 II medium (Invitrogen); the multiplicity of infection was ~5. After 60 h of infection, medium containing secreted ATX was collected by low speed centrifugation and applied onto a Q-Sepharose column (Amersham Biosciences). The flow-through was applied onto a hydroxyapatite column (Bio-Rad), and the bound proteins were eluted with a linear potassium phosphate gradient. The ATX-containing fractions were applied onto an isopropyl column (Amersham Biosciences), and bound proteins were eluted with a decreasing linear gradient of ammonium sulfate. Purity of ATX-containing fractions was > 95% as shown by SDS-PAGE and Coomassie Blue staining. The approximate yield was about 3 mg of pure protein from 10 liters of culture supernatant.

Recombinant NPP1—A soluble secreted form of human NPP1 was made by in-frame ligation of its extracellular domain to the BamHI site

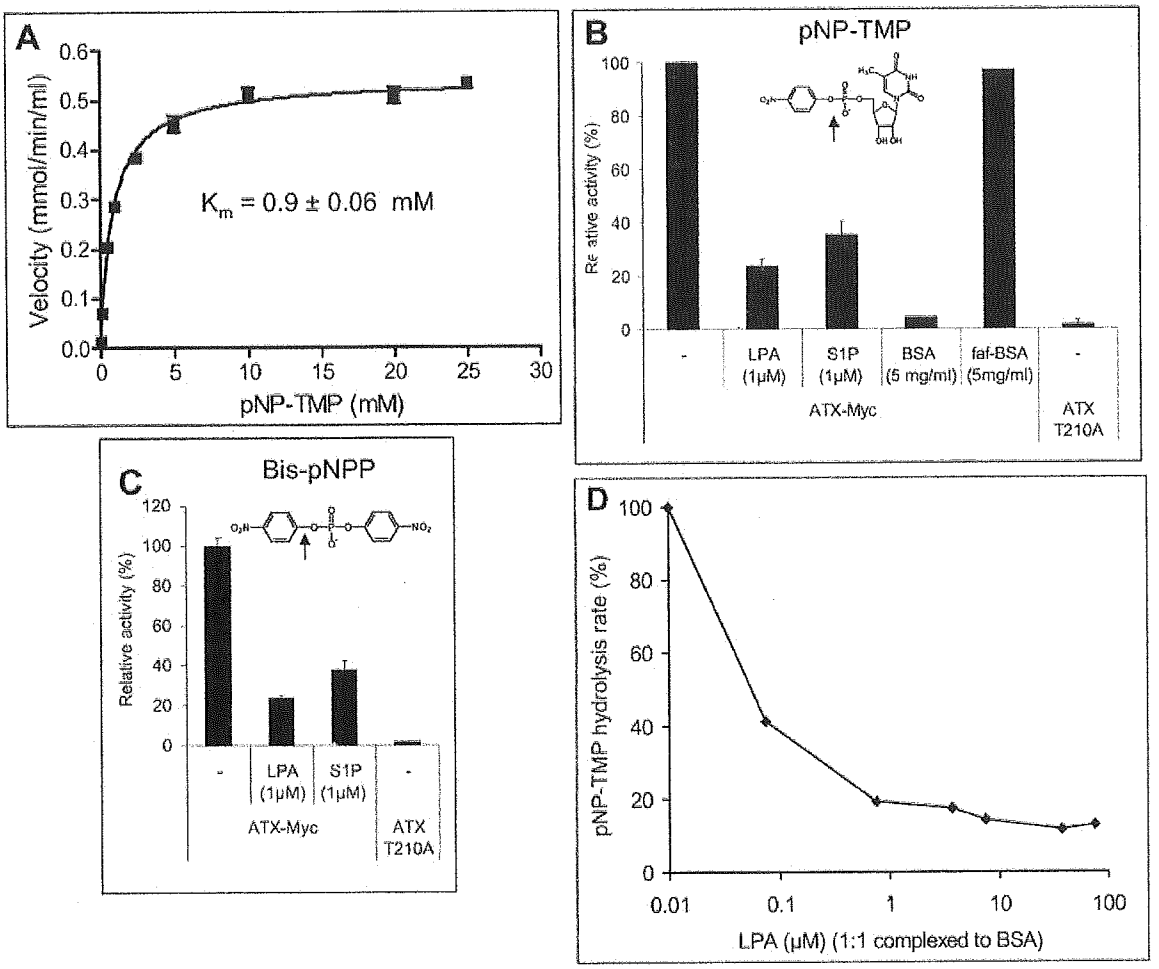

FIG. 3. **ATX-catalyzed hydrolysis of non-lipid substrates.** *A*, hydrolysis of pNP-TMP. Initial rates of pNP formation, measured over 3 h by light absorbance, are plotted against increasing substrate concentrations and fitted according to the Michaelis-Menten equation using GraphPad software. *B*, hydrolysis of pNP-TMP (1 mM). LPA (1-oleoyl) and S1P were added at 1 μM. BSA and delipidated BSA (*faf-BSA*; 99% fatty acid-free) were added at 5 mg/ml. *ATX T210A* represents catalytically inactive ATX. *Inset*, structure of pNP-TMP; *arrow* indicates the phosphodiesterase cleavage site. *C*, hydrolysis of bis-pNPP (1 mM). LPA and S1P were added at 1 μM. *Inset*, structure of bis-pNPP; *arrow* indicates the phosphodiesterase cleavage site. *D*, inhibition of pNP-TMP hydrolysis by increasing concentrations of 1-oleoyl-LPA, complexed to delipidated BSA (1:1 molar ratio). pNP-TMP was used at 1 mM.

of the cleavable signal sequence from influenza hemagglutinin, and cloned into a mammalian expression vector driven by the SR-α promoter. After linearization, the DNA was transfected into Chinese hamster ovary cells, and a highly expressing stable transfectant was isolated by single cell cloning. The soluble enzyme was purified from culture supernatants by sequential chromatography consisting of large scale anion exchange chromatography, Blue-Sepharose, AMP-Sepharose, and final polishing on a Uno-Q column (Bio-Rad). Purity was confirmed by SDS-PAGE and silver staining.

lyso-PLD Assay—To measure lyso-PLD activity, radiolabeled LPC (1-[1-^{14}C]palmitoyl, Amersham Biosciences) and unlabeled LPC (1 μM) were dried under nitrogen, and the mixture was reconstituted in Tris-buffered saline (140 mM NaCl, 5 mM KCl, 1 mM $CaCl_2$, 1 mM $MgCl_2$, adn 50 mM Tris, pH 8.0) and sonicated, and BSA (2 mg/ml) was added. The reaction was started by the addition of ATX-containing conditioned medium. Lipids were extracted with butan-1-ol. All of the solutions were made 0.02 M in acetic acid and extracted with 0.5 volume of butan-1-ol as described previously (22). In brief, after thorough mixing and centrifugation, the butan-1-ol phase was removed, and the water phase was extracted once again. Butanol fractions were washed with 1 volume of butan-1-ol-saturated water and dried under nitrogen. Phospholipids were separated by thin layer chromatography on silica gel-60 plates in chloroform/methanol/acetic acid/water (50:30:8:4). Lipids were detected by autoradiography.

Phosphodiesterase Assays—Phosphodiesterase activity toward pNP-TMP and bis-pNPP was measured by light absorbance. 40 μl of HEK293T-conditioned medium was added to 160 μl of Tris-buffered saline (140 mM NaCl, 5 mM KCl, 1 mM $CaCl_2$, 1 mM $MgCl_2$, and 50 mM Tris, pH 8.0) containing pNP-TMP or bis-pNPP in 96-well plates. After incubation for 3 h at 37 °C, the amount of liberated *para*-nitrophenolate (pNP) was determined by reading the absorbance at 405 nm in a Victor Wallac plate reader.

CPF4 FRET Assay—CPF4 was synthesized as described previously (26) and maintained as a 10-mM stock solution in Me_2SO. Recombinant ATX in Tris-buffered saline (140 mM NaCl, 5 mM KCl, 1 mM $CaCl_2$, 1 mM $MgCl_2$, 50 mM Tris, pH 8.0) or ATX-Myc-containing conditioned Dulbecco's modified Eagle's medium (buffered with 50 mM Tris, pH 8.0) was incubated with or without the indicated reagents, and CPF4 was added at a concentration of 2 μM unless indicated otherwise. CPF4 fluorescence was monitored (at 37 °C) in a BMG Fluorstar 96-well plate reader (excitation at 355 nm, emission at 460 and 520 nm). Curve fitting was carried out using GraphPad software.

Fluorescence Microscopy—Cells transfected with ATX-GFP or LPA_1-GFP (28) were fixed with ice-cold methanol at 24 h after transfection. ATX and LPA_1 were detected by anti-GFP antibody using a Leica confocal microscope.

RESULTS AND DISCUSSION

ATX Processing in HEK293 Cells—ATX is synthesized as a type II transmembrane glycoprotein of ~125 kDa, consisting of a very short N-terminal region, a single transmembrane domain, and a large catalytic ectodomain. ATX undergoes membrane-proximal cleavage to yield a soluble enzyme (29), yet

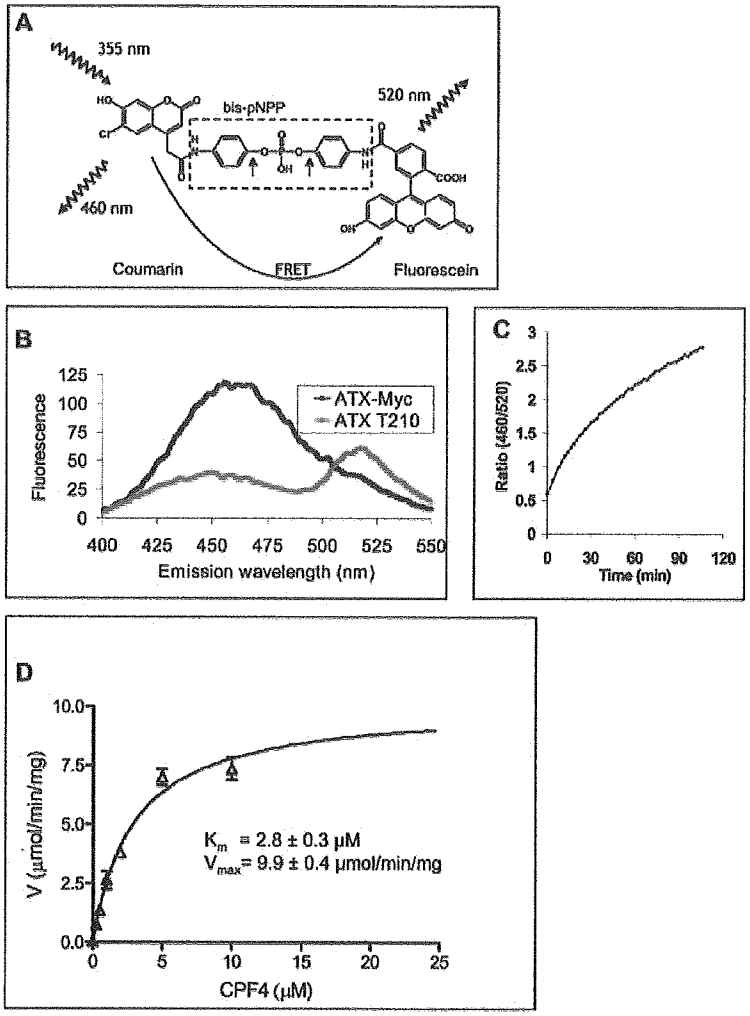

FIG. 4. **FRET-based biosensor CPF4 as an ATX substrate.** *A*, the structure of CPF4 and the mechanism of FRET (for details see Ref. 26). *B*, loss of CPF4 FRET induced by ATX-Myc, as detected by an increase in donor fluorescence and a decrease in acceptor fluorescence (*blue trace*). CPF4 concentration, 2 μM. The inactive mutant ATX(T210A)-Myc served as a negative control (*red trace*). *C*, time-dependent increase in loss of FRET induced by ATX, detected as an increase in the ratio between the fluorescence of the donor and that of the acceptor. CPF4 concentration, 2 μM. *D*, saturation kinetics of CPF4 hydrolysis by purified recombinant ATX. CPF4 hydrolysis by ATX-Myc in conditioned medium shows the same saturation kinetics (see Fig. 6).

little is known about ATX biosynthesis and proteolytic processing. In particular, it remains unclear whether the transmembrane form of ATX is expressed on the cell surface.

As a starting point for the present studies, we expressed full-length ATX in HEK293T cells using three differently HA- and Myc-tagged constructs and analyzed ATX expression in cell lysates as well as in the culture medium. As shown in Fig. 1*A*, full-length ATX is detected only in cell lysates, whereas ATX in the medium lacks the N-terminal HA tag, consistent with secreted ATX being produced by cleavage of the N terminus. The Golgi-disturbing agents brefeldin A and monensin blocked ATX secretion, indicating involvement of the classical export route (supplemental Fig. 1*A*). When analyzed by confocal microscopy, ATX is detected in intracellular vesicles but not at the plasma membrane; in contrast, LPA_1 receptors localize primarily to the cell surface under the same experimental conditions (Fig. 1*B*). From these results we conclude that ATX follows the classical secretory pathway and that proteolytic removal of its N terminus, including the transmembrane region, occurs intracellularly rather than at the plasma membrane.

ATX Activity toward Lipid and Non-lipid Substrates—Having established that ATX is not detectable as a plasma membrane-anchored ecto-enzyme, we set out to examine the catalytic activity of soluble ATX. To this end, we used conditioned medium from ATX-Myc-transfected HEK293T cells without further purification or, in some experiments, ATX purified from Sf9 cell supernatant (supplemental Fig. 1*B*). The catalytically inactive mutant ATX(T210A) served as a negative control (27).

The lyso-PLD activity of ATX was measured by the conversion of LPC(16:0) to LPA using thin layer chromatograpy (Fig. 2*A*). LPC hydrolysis by ATX proceeded at a constant rate for at least 90 min (Fig. 2*C*, *left panel*). The K_m for LPC was estimated at ~150 μM, in agreement with previously reported values (100–260 μM) (11, 12, 14) and in the range of normal LPC levels in plasma (25). When screening multiple lipids as potential modulators of lyso-PLD activity, we observed that ATX-catalyzed LPC hydrolysis was significantly inhibited by LPA and S1P (1 μM, complexed to albumin). Other phospholipids tested, including phosphatidic acid, did not show such an effect (Fig. 2 and results not shown). This suggests that ATX is subject to product inhibition by LPA. Detailed analysis of lyso-PLD inhibition is obscured, however, by limitations with the standard LPC hydrolysis assay, which generates concentrations of LPA in excess of its inhibition constant (see below). As a result, formation of LPA during the course of the assay causes the apparent inhibition of ATX by added LPA to be less pronounced than the true inhibition.

To avoid the complications of lipid product inhibition and the limitations of end-point LPC hydrolysis assays, we took advantage of the fact that ATX uses a common reaction mechanism for the hydrolysis of lipid and non-lipid substrates (20, 21). As non-lipid substrates, we tested pNP-TMP, a standard NPP substrate, and the symmetric phosphodiester bis-pNPP, a sub-

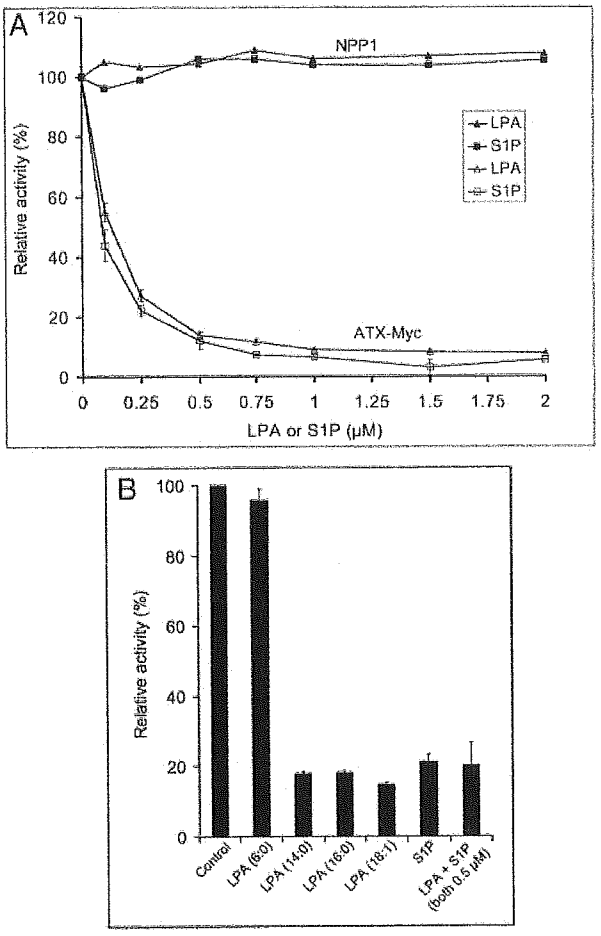

FIG. 5. **ATX inhibition by LPA and S1P.** *A*, dose-response curves for the inhibitory effects of LPA (1-oleoyl) and S1P on the activity of ATX-Myc and purified NPP1 (about 2 μg/100 μl of assay volume). CFP4 concentration, 2 μM. *B*, dependence of ATX inhibition on the acyl chain length of LPA (1 μM). The *rightmost* bar shows that the inhibitory effects of LPA and S1P (both added at 0.5 μM) are not additive.

strate for type I phosphodiesterases and certain bacterial PLDs (30–32). The liberated product, pNP, was quantified colorimetrically. As shown in Fig. 3*A*, hydrolysis of pNP-TMP followed Michaelis-Menten kinetics with a K_m of 0.9 mM, somewhat lower than the value reported by others (12). ATX was also capable of hydrolyzing bis-pNPP (Fig. 3*C*), in keeping with a previous report (21). bis-pNPP hydrolysis rates were half-maximal at ~0.5 mM but did not obey Michaelis-Menten kinetics, apparently because of substrate inhibition at higher concentrations (>1 mM; results not shown).

Similar to what is observed with LPC as a substrate, the hydrolysis of pNP-TMP and bis-pNPP by ATX was significantly inhibited by LPA and S1P (1 μM) (Fig. 3, *B* and *C*). It thus appears that, importantly, LPA and S1P exert their inhibitory effect regardless of the nature of the substrate.

Effects of BSA—Using pNP-TMP as a substrate, we observed that ATX activity was strongly inhibited by normal serum albumin (BSA) at concentrations of >50 μg/ml (0.75 μM; ~0.1% of the concentration in fetal calf serum). In marked contrast, delipidated BSA (Fig. 3*B*, *faf-BSA*) had no inhibitory effect, even when added at high concentrations (5 mg/ml; 75 μM). The observation that albumin is the major binding protein for LPA and S1P strongly suggests that ATX inhibition by "normal" BSA is largely due to these lysophospholipids. When LPA was complexed to delipidated albumin (at a 1:1 molar ratio), we found that its ability to inhibit ATX was not affected. As can be inferred from Fig. 3*D*, the IC_{50} value for the LPA·BSA (1:1) complex to inhibit ATX was close to 0.1 μM, using a substrate concentration of 1 mM (*i.e.* equal to the K_m).

CPF4, a FRET-based Sensor of ATX Activity—Because the pNP-TMP colorimetric assay showed only moderate sensitivity (detection limit, ~0.15 μg of ATX/ml), we explored a newly developed FRET-based phosphodiesterase sensor termed CPF4 (26). CPF4 is a bis-pNPP-derived probe, in which both phenyl moieties are linked to coumarin and fluorescein, respectively, resulting in FRET with high efficiency (Fig. 4*A*). Cleavage of the phosphodiester group by a nonspecific phosphodiesterase from snake venom causes loss of FRET, providing a convenient ratiometric readout of enzyme activity (26). Notably, the CPF4 fluorescence ratio is insensitive to pH in the physiological range (pH 7.0–8.0) (26). A major advantage of fluorescence-based sensors like CPF4 is their high sensitivity, allowing detection of very low concentrations of enzyme.

We examined whether CPF4 serves as a substrate for ATX. As shown in Fig. 4*B*, ATX-Myc causes a prominent loss of FRET (increased donor fluorescence and a concomitant decrease in acceptor fluorescence), indicative of substrate hydrolysis, which can be monitored in real time (Fig. 4*C*). No CFP4 signal change was detected with the inactive mutant ATX(T210A). A plot of the initial hydrolysis rates *versus* CPF4 concentration revealed Michaelis-Menten kinetics with an average K_m as low as ~4 μM (range, 2.5–6 μM) for ATX-Myc in HEK293 cell-conditioned medium (Fig. 4*D*). About the same K_m value was found with highly purified ATX from Sf9 cell supernatant (see below and Fig. 6), suggesting that conditioned medium does not contain significant amounts of competitive inhibitors of ATX (which would increase the apparent K_m).

It is noteworthy that the apparent affinity of ATX for CPF4 is 2–3 orders of magnitude higher than that for lysophospholipids and nucleotides (K_m = 0.1–1.0 mM; one notable exception is diadenosine triphosphate with an apparent K_m of 8 μM (33)). Also with bis-pNPP, a "non-Michaelis-Menten" substrate, half-maximal hydrolysis rates are observed at concentrations as high as ~0.5 mM. Thus attachment of the coumarin-fluorescein tandem to bis-pNPP, which increases hydrophobicity and disturbs structural symmetry, converts bis-pNPP into a high-affinity substrate for ATX, suggesting that the coumarin-fluorescein tandem fits into a hydrophobic pocket involved in substrate binding. Although the overall catalytic efficiency (V_{max}/K_m) of CPF4 hydrolysis was about 3-fold lower than that observed with the other substrates, the FRET-based assay showed superior sensitivity; even at a 5000-fold dilution of HEK293T cell-conditioned medium, ATX activity was still detectable. The estimated detection limit of the CFP4 assay was 3 ng of ATX/ml, exceeding that of the standard colorimetric assay by at least 50-fold. This makes CPF4 the preferred probe for measuring ATX activity in conditioned media and body fluids, although it remains to be seen to what extent the presence of binding proteins and/or nonspecific phosphodiesterases may limit the usefulness of CPF4 in assessing ATX activity in complex biological fluids.

We also examined whether CPF4 is a substrate for nonmammalian secreted lyso-PLDs, notably the broad specificity PLD from *S. chromofuscus* and the sphingomyelin- and LPC-specific PLDs from *C. pseudotuberculosis* and *Loxosceles laeta* (28). When assayed under the conditions used for ATX, none of these exogenous PLDs (10 nM) was able to cleave CPF4 (results not shown). It thus appears that among the known secreted PLDs, only ATX can hydrolyze CPF4.

Inhibition of ATX by LPA and S1P—Because of its superior sensitivity and convenient readout, the CPF4 assay was used

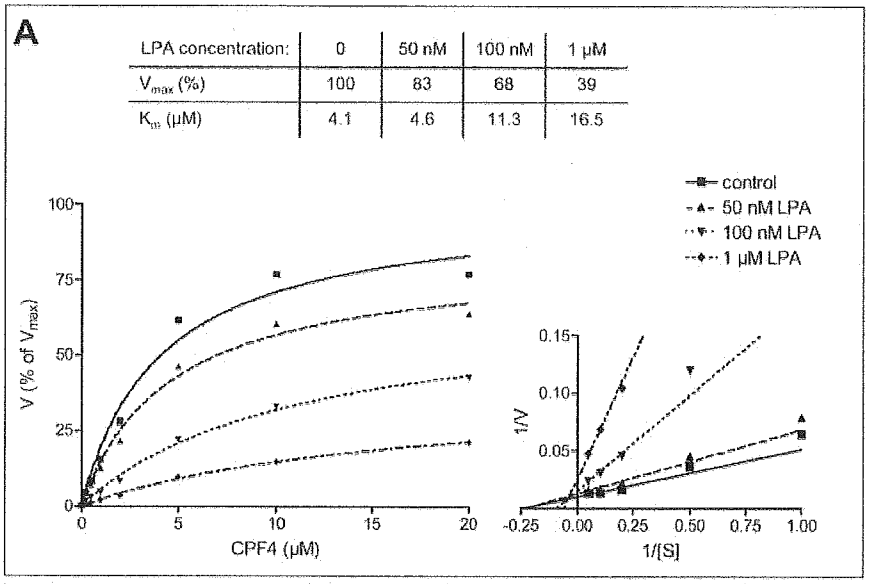

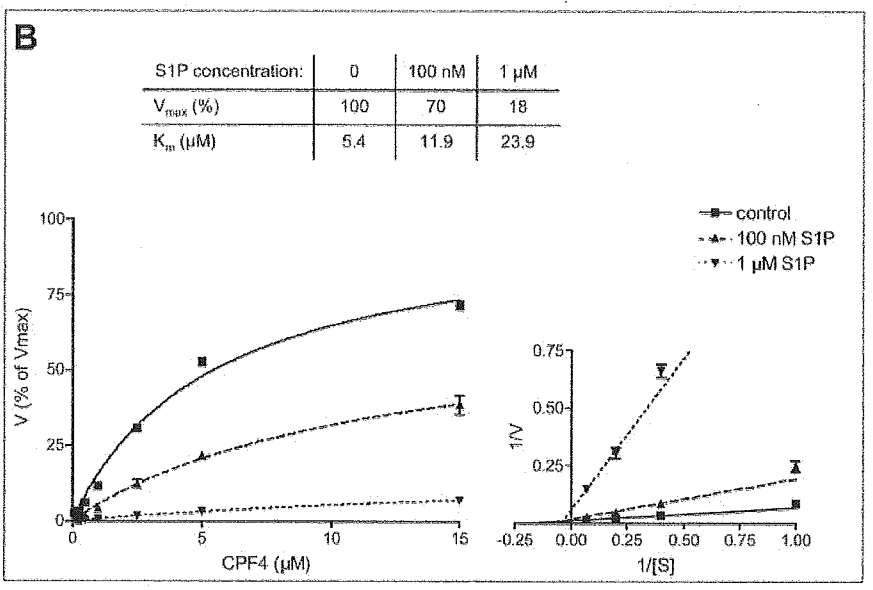

FIG. 6. **Kinetic analysis of ATX inhibition by LPA and S1P.** Inhibition of ATX-Myc by 1-oleoyl-LPA (*A*) and S1P (*B*) added at the indicated concentrations. Inhibition by LPA and S1P produces a decrease in V_{max} and an increase in K_m, indicative of "mixed-type" inhibition. Similar results were obtained with purified recombinant ATX (not shown).

in our further analysis of ATX inhibition. We determined the concentration dependence of LPA and S1P for inhibiting ATX activity using a substrate concentration close to the K_m. Under those conditions, the IC_{50} value for 1-oleoyl-LPA is ~0.1 μM (Fig. 5*A*), very similar to the value found with pNP-TMP or LPC as substrate (Fig. 3*D* and results not shown). S1P inhibited ATX activity with the same dose dependence as observed for LPA (Fig. 5*A*). Other natural lipids, including dioleoylphosphatidic acid, 1-oleoyl-glycerol, sphingosine (10 mM), glycerol 3-phosphate (1 mM), and free fatty acids, did not affect ATX activity. Although AMP has been reported to inhibit the NPP reaction (1, 2), we did not observe any effect of either AMP or ATP (1 mM) on ATX activity (results not shown).

Importantly, the inhibitory effects of LPA and S1P were specific for ATX in that the activity of the structurally related ecto-phosphodiesterase NPP1 was insensitive to either lipid (Fig. 5*A*). Inhibition of ATX by LPA was dependent on the length of the acyl chain; maximal inhibition was induced by 1-oleoyl-LPA, 1-palmitoyl-LPA, and 1-myristoyl-LPA, whereas short-chain LPA(6:0) had no measurable effect (Fig. 5*B*). The apparent requirement of a long acyl chain suggests that LPA and S1P directly interact with a hydrophobic pocket on ATX. The inhibitory effects of LPA and S1P were nonadditive (Fig. 5*B*), suggesting that both lipids act on the same regulatory site. We conclude that, in marked contrast to the G protein-coupled receptors (17), ATX does not discriminate between LPA and S1P as ligands.

We next examined the mechanism of inhibition by LPA and S1P. Substrate titration studies revealed that LPA and S1P are mixed-type inhibitors, producing a reduction in V_{max} and an increase in K_m (Fig. 6). In other words, inhibition of ATX by LPA/S1P has both a noncompetitive and a competitive compo-

nent, resulting from a combination of a decreased turnover number and decreased affinity of the active site for its substrates. Double-reciprocal plot analysis (Fig. 6) yielded an inhibition constant (K_i) of 110 nM for LPA and 50 nM for S1P, values well within the biologically active range of LPA and S1P. We note that these K_i values are ~1000-fold lower than the reported K_m for the LPC substrate (100–200 μM) (11, 12, 14), indicating that ATX binds LPA and S1P much more strongly than it binds its physiological substrate(s).

Conclusion—We have employed a novel and highly sensitive FRET-based phosphodiesterase sensor to show that the catalytic activity of ATX, secreted by the classical export pathway, is potently and specifically inhibited by LPA and S1P. Kinetic analysis revealed that LPA and S1P act as mixed-type inhibitors with an inhibition constant (K_i) of ~0.1 μM. The inhibition of ATX by LPA and S1P is specific in that (i) short-chain LPA(6:0) and other lipids have no effect, and (ii) the closely related ecto-phosphodiesterase NPP1, which lacks lyso-PLD activity, is insensitive to LPA and S1P. Because ATX primarily functions as an LPA-generating lyso-PLD, our findings imply that LPA is capable of controlling its own biosynthesis in the cellular environment. Product inhibition of ATX will prevent excessive accumulation of bioactive LPA in the extracellular milieu and may explain why steady-state plasma levels of LPA are very low despite the abundance of its precursor LPC. That serum LPA levels rapidly increase following platelet activation (24) suggests that plasma ATX may also be positively regulated by as yet unknown factors, an important issue that needs to be further explored.

Our findings point to a novel role for S1P as an inhibitor of ATX, in addition to its well documented role as a receptor agonist. The important implication is that changes in extracellular S1P levels may greatly influence LPA production and signaling. Because the S1P concentrations in blood are significant (16, 34), close to the inhibition constant for ATX reported here (~ 0.1 μM), ATX activity in plasma could be permanently suppressed by S1P under basal conditions. Our results further imply that ATX has a unique binding site for LPA and S1P, not present in NPP1. Interestingly, a photo-affinity labeling study has shown that, in addition to its catalytic site, ATX contains an isoform-specific sequence that can be cross-linked to ATP (35). Mutagenesis experiments, in combination with structural studies, should reveal whether this second nucleotide-binding region is in fact an allosteric site for LPA and S1P. Identification and characterization of the LPA/S1P binding site(s) is a major challenge for future studies and will likely facilitate the development of selective ATX inhibitors that could be of value in anticancer therapy.

Acknowledgments—We thank Ben Giepmans for help with cDNA cloning and Mary Roberts, Denise Tambourgi, and Steve Billington for purified PLDs.

REFERENCES

1. Bollen, M., Gijsbers, R., Ceulemans, H., Stalmans, W., and Stefan, C. (2000) *Crit. Rev. Biochem. Mol. Biol.* **35,** 393–432
2. Clair, T., Lee, H. Y., Liotta, L. A., and Stracke, M. L. (1997) *J. Biol. Chem.* **272,** 996–1001
3. Goding, J. W., Grobben, B., and Slegers, H. (2003) *Biochim. Biophys. Acta* **1638,** 1–19
4. Stracke, M. L., Krutzsch, H. C., Unsworth, E. J., Arestad, A., Cioce, V., Schiffmann, E., and Liotta, L. A. (1992) *J. Biol. Chem.* **267,** 2524–2529
5. Murata, J., Lee, H. Y., Clair, T., Krutzsch, H. C., Arestad, A. A., Sobel, M. E., Liotta, L. A., and Stracke, M. L. (1994) *J. Biol. Chem.* **269,** 30479–30484
6. Nam, S. W., Clair, T., Campo, C. K., Lee, H. Y., Liotta, L. A., and Stracke, M. L. (2000) *Oncogene* **19,** 241–247
7. Nam, S. W., Clair, T., Kim, Y. S., McMarlin, A., Schiffmann, E., Liotta, L. A., and Stracke, M. L. (2001) *Cancer Res.* **61,** 6938–6944
8. Mills, G. B., and Moolenaar, W. H. (2003) *Nat. Rev. Cancer* **3,** 582–591
9. Fuss, B., Baba, H., Phan, T., Tuohy, V. K., and Macklin, W. B. (1997) *J. Neurosci.* **17,** 9095–9103
10. Bachner, D., Ahrens, M., Betat, N., Schroder, D., and Gross, G. (1999) *Mech. Dev.* **84,** 121–125
11. Umezu-Goto, M., Kishi, Y., Taira, A., Hama, K., Dohmae, N., Takio, K., Yamori, T., Mills, G. B., Inoue, K., Aoki, J., and Arai, H. (2002) *J. Cell Biol.* **158,** 227–233
12. Tokumura, A., Majima, E., Kariya, Y., Tominaga, K., Kogure, K., Yasuda, K., and Fukuzawa, K. (2002) *J. Biol. Chem.* **277,** 39436–39442
13. Moolenaar, W. H., van Meeteren, L. A., and Giepmans, B. N. (2004) *BioEssays* **26,** 870–881
14. Clair, T., Aoki, J., Koh, E., Bandle, R. W., Nam, S. W., Ptaszynska, M. M., Mills, G. B., Schiffmann, E., Liotta, L. A., and Stracke, M. L. (2003) *Cancer Res.* **63,** 5446–5453
15. Postma, F. R., Jalink, K., Hengeveld, T., and Moolenaar, W. H. (1996) *EMBO J.* **15,** 2388–2392
16. Hla, T., Lee, M. J., Ancellin, N., Paik, J. H., and Kluk, M. J. (2001) *Science* **294,** 1875–1878
17. Ishii, I., Fukushima, N., Ye, X., and Chun, J. (2004) *Annu. Rev. Biochem.* **73,** 321–354
18. Liliom, K., Sun, G., Bunemann, M., Virag, T., Nusser, N., Baker, D. L., Wang, D. A., Fabian, M. J., Brandts, B., Bender, K., Eickel, A., Malik, K. U., Miller, D. D., Desiderio, D. M., Tigyi, G., and Pott, L. (2001) *Biochem. J.* **355,** 189–197
19. Spiegel, S., and Milstien, S. (2003) *Nat. Rev. Mol. Cell. Biol.* **4,** 397–407
20. Koh, E., Clair, T., Woodhouse, E. C., Schiffmann, E., Liotta, L., and Stracke, M. (2003) *Cancer Res.* **63,** 2042–2045
21. Gijsbers, R., Aoki, J., Arai, H., and Bollen, M. (2003) *FEBS Lett.* **538,** 60–64
22. Eichholtz, T., Jalink, K., Fahrenfort, I., and Moolenaar, W. H. (1993) *Biochem. J.* **291,** 677–680
23. Baker, D. L., Morrison, P., Miller, B., Riely, C. A., Tolley, B., Westermann, A. M., Bonfrer, J. M., Bais, E., Moolenaar, W. H., and Tigyi, G. (2002) *J. Am. Med. Assoc.* **287,** 3081–3082
24. Sano, T., Baker, D., Virag, T., Wada, A., Yatomi, Y., Kobayashi, T., Igarashi, Y., and Tigyi, G. (2002) *J. Biol. Chem.* **277,** 21197–21206
25. Croset, M., Brossard, N., Polette, A., and Lagarde, M. (2000) *Biochem. J.* **345,** 61–67
26. Takakusa, H., Kikuchi, K., Urano, Y., Sakamoto, S., Yamaguchi, K., and Nagano, T. (2002) *J. Am. Chem. Soc.* **124,** 1653–1657
27. Lee, H. Y., Clair, T., Mulvaney, P. T., Woodhouse, E. C., Aznavoorian, S., Liotta, L. A., and Stracke, M. L. (1996) *J. Biol. Chem.* **271,** 24408–24412
28. van Meeteren, L. A., Frederiks, F., Giepmans, B. N., Pedrosa, M. F., Billington, S. J., Jost, B. H., Tambourgi, D. V., and Moolenaar, W. H. (2004) *J. Biol. Chem.* **279,** 10833–10836
29. Stracke, M. L., Clair, T., and Liotta, L. A. (1997) *Adv. Enzyme Regul.* **37,** 135–144
30. Kelly, S. J., Dardinger, D. E., and Butler, L. G. (1975) *Biochemistry* **14,** 4983–4988
31. Rudolph, A. E., Stuckey, J. A., Zhao, Y., Matthews, H. R., Patton, W. A., Moss, J., and Dixon, J. E. (1999) *J. Biol. Chem.* **274,** 11824–11831
32. Zambonelli, C., Casali, M., and Roberts, M. F. (2003) *J. Biol. Chem.* **278,** 52282–52289
33. Vollmayer, P., Clair, T., Goding, J. W., Sano, K., Servos, J., and Zimmermann, H. (2003) *Eur. J. Biochem.* **270,** 2971–2978
34. Yang, L., Yatomi, Y., Miura, Y., Satoh, K., and Ozaki, Y. (1999) *Br. J. Haematol.* **107,** 282–293
35. Clair, T., Krutzsch, H. C., Liotta, L. A., and Stracke, M. L. (1997) *Biochem. Biophys. Res. Commun.* **236,** 449–454

Available online at www.sciencedirect.com
SCIENCE DIRECT®
Archives of Biochemistry and Biophysics 442 (2005) 222–228
ABB
www.elsevier.com/locate/yabbi

Evidence for pH dependent Zn^{2+} influx in K562 erythroleukemia cells: Studies using ZnAF-2F fluorescence and $^{65}Zn^{2+}$ uptake

Robert A. Colvin [a,*], Charles P. Fontaine [a], Dustin Thomas [a], Tomoya Hirano [b], Tetsuo Nagano [b], Kazuya Kikuchi [b]

[a] *Department of Biological Sciences, OHIO University, Athens, OH 45701, USA*
[b] *Graduate School of Pharmaceutical Sciences, The University of Tokyo, Tokyo, Japan*

Received 10 July 2005, and in revised form 17 August 2005
Available online 8 September 2005

Abstract

Using both ZnAF-2F (a Zn^{2+} specific fluorophore) and $^{65}Zn^{2+}$, we determined the rate of transporter mediated Zn^{2+} influx (presumably mediated by the SLC39A1 gene product, protein name hZIP1) under steady state conditions and studied the effects of extracellular acidification. When K562 erythroleukemia cells were placed in Zn^{2+} containing buffers (1–60 μM), the initial rate of $^{65}Zn^{2+}$ accumulation mirrored the apparent rise in free intracellular Zn^{2+} concentrations sensed by ZnAF-2F. Therefore, newly transported Zn^{2+} equilibrated with the free intracellular Zn^{2+} pool sensed by ZnAF-2F. A new steady state with elevated free intracellular Zn^{2+} was established after about 30 min. An estimate of 11 μM for the K_m and 0.203 nmol/mg/s for the V_{max} were obtained for Zn^{2+} influx. $^{65}Zn^{2+}$ uptake and ZnAF-2F fluorescent changes were inhibited by extracellular acidification (range tested: pH 8–6, IC_{50} = pH 6.34). The IC_{50} for proton effects was close to the pK_a for histidine, suggesting conserved histidine residues present in SLC39A1 play a critical role in Zn^{2+} influx and are involved in the pH effect.

Keywords: Metal ion transport; Zinc homeostasis; Fluorescence

Using currently available genomic data and analyses from several eukaryotic organisms, Zn^{2+} transporters appear to fall into two distinct gene families named SLC39 (protein name: ZIP) [1,2] and SLC30 (protein name: ZnT) [3]. Functional characterization of the mammalian SLC39 family members (hZIP-1, -2, and -4) provides convincing support for the notion that SLC39 proteins are targeted to the plasma membrane and are involved primarily in cellular Zn^{2+} influx [4–7]. SLC39 proteins appear to mediate a facilitated diffusion of Zn^{2+}, driven primarily by the concentration gradient for Zn^{2+} across the plasma membrane. No evidence exists for an energy requirement, effect of membrane potential, or the cotransport of other ions, except perhaps bicarbonate (SLC39A2 only) [4,5]. Thus, very little is known concerning the mechanism of Zn^{2+} influx. One recent study suggests that SLC39 proteins move ligand bound Zn^{2+} across the plasma membrane (rather than free Zn^{2+}) [8], the implication being that Zn^{2+} added in solution is a poor measure of the protein's true affinity for Zn^{2+}.

The function, tissue location, and mechanism of Zn^{2+} transport by SLC30 family members are best studied for the product of the mammalian gene SLC30A1 (ZnT-1) and its several homologs. [9]. SLC30A1 is ubiquitously expressed and likely to be involved in Zn^{2+} efflux. For example, PC-12 cells expressing SLC30A1 show increased Zn^{2+} efflux and reduced sensitivity to Zn^{2+} induced cell death [10]. The remaining SLC30 family members are preferentially localized to intracellular membranes where they have more limited, tissue specific expression, probably related to physiological intracellular Zn^{2+} compartmentalization [11–16]. Several studies [5,9,14–16] support a division of labor between Zn^{2+} transporters. Thus, SLC39 family members

* Corresponding author. Fax: +1 740 593 0300.
E-mail address: colvin@ohio.edu (R.A. Colvin).

0003-9861/$ - see front matter © 2005 Elsevier Inc. All rights reserved.
doi:10.1016/j.abb.2005.08.013

are responsible for Zn^{2+} influx and SLC30 family members are involved in Zn^{2+} efflux and intracellular compartmentalization. This leads to a model predicting that under steady state conditions, free intracellular Zn^{2+} concentrations are maintained by a balance between the rate of separate and distinct Zn^{2+} influx and efflux mechanisms across the plasma membrane and exchange with sequestered Zn^{2+} pools inside the cell. However, direct experimental proof of this model in mammalian cells is lacking at present.

Our laboratory is studying Zn^{2+} transport using cultured cells in hopes of addressing questions of transport mechanism and the role of mammalian Zn^{2+} transporters in cellular homeostasis. One of our consistent findings is an inhibition of $^{65}Zn^{2+}$ uptake by extracellular acidification. In addition, we have shown that intracellular acidification of cortical neurons results in a stimulation of $^{65}Zn^{2+}$ uptake [17,18]. These data have led us to hypothesize that protons are fundamental to the uptake mechanism and the pH effect could reflect an antiport mechanism of coupled Zn^{2+}/proton transport. Unfortunately, no experimental evidence exists linking protons to the transport mechanisms of either SLC30 or SLC39 family members. To address issues of cellular Zn^{2+} homeostasis and the mechanism(s) of Zn^{2+} transport, we used a model cell system (K562 erythroleukemia cells) with well characterized Zn^{2+} uptake transporter function and two complimentary techniques—ZnAF-2F fluorescence and $^{65}Zn^{2+}$ uptake. These studies allowed us to measure initial rates of Zn^{2+} influx and measure changes in steady state intracellular Zn^{2+} levels. Our data suggests that SLC39A1 (hZIP1) transport function was inhibited by extracellular acidification.

Materials and methods

Culture of K562 erythroleukemia cells

K562 erythroleukemia cells (#CCL-243) were obtained from American Type Culture Collection (Manassas, VA). Cells were maintained in complete RPMI 1640 medium (Life Technologies), supplemented with 2 mM glutamine and 10% fetal bovine serum (Atlas Biologicals, Fort Collins, CO) with 500 ng/ml Gentamicin and 250 ng/ml Fungizone (Life Technologies) added. Cells were grown in suspension in 25 cm^2 flasks at 37 °C in a 5% CO_2 incubator. When necessary, cells were allowed to attach to poly-D-lysine (0.1 mg/ml in borate buffer) coated coverslips overnight. Approximately, 5×10^4 cells were applied to each coverslip. This quantity of cells per coverslip provides an optimal fluorescent signal when using ZnAF-2F.

$^{65}Zn^{2+}$ flux measurements

Experiments were performed similar to those described previously [17]. K562 cells were first harvested by centrifugation (5 min at 500 rpm—Beckman Allegra 25R centrifuge) and then resuspended in Locke's buffer (154 mM NaCl, 5.6 mM KCl, 2.3 mM $CaCl_2$, 1.0 mM $MgCl_2$, 5 mM Hepes, and 10 mM glucose). The cell suspension was then assayed for protein by the Bio-Rad method using bovine serum albumin as the standard. The cells were then diluted to a concentration of 1.5–2.0 mg/ml. Locke's buffers (bubbled with O_2 to remove dissolved CO_2) containing $^{65}Zn^{2+}$ (Los Alamos National Laboratory, NM) were prepared by adding various amounts of 1 mM $^{65}Zn^{2+}$ (0.01–0.02 μCi/μl). Transport reactions were initiated by adding 0.225 ml of prewarmed (37 °C) buffer to .025 ml of cell suspension in a 37 °C water bath. After various times, the reaction tubes were removed from the water bath and immediately placed in ice to stop the transport reaction. Cell suspensions were rapidly filtered on GF/C filter paper using a Brandel cell harvester and washed 3 times with ice-cold buffer containing 137 mM cholineCl/10 mM Hepes, pH 7.4/1 mM EGTA. When initial velocity experiments were performed, the transport reactions were stopped by filtration. The radioactivity caught on the filters was determined by liquid scintillation counting. As total Zn^{2+} added to the buffers was known ($^{65}Zn^{2+}$ plus nonradioactive Zn^{2+}), aliquots of the uptake buffer were counted for radioactivity to determine the specific activity of $^{65}Zn^{2+}$. Using this value, the counts on the filter were converted to nanomoles of Zn^{2+} per milligram protein.

SNARF-1 fluorescence and acidification

K562 cells attached to poly-D-lysine coated glass coverslips were loaded with SNARF-1 by incubation for 30 min in Locke's buffer (pH 7.4) at 37 °C containing 5 μM 5-(and-6)-carboxy SNARF-1, acetoxymethyl ester, acetate (Molecular Probes, Eugene, OR) [17]. The cells were then washed with 1 ml of Locke's buffer prior to pH measurement. The cells were then placed on ice until being used for an experiment. Cells attached to coverslips were held in a cuvette at approximately a 45° angle to the incident light beam by a coverslip holder (Hitachi Instruments, San Jose, CA). To measure fluorescence changes, the cuvette/coverslip holder was placed in the fluorescence spectrophotometer (Hitachi F-2000). To switch buffer solutions, the coverslip and holder were lifted out of the cuvette and quickly placed into a waiting cuvette containing the next desired buffer. SNARF-1 fluorescence was measured using excitation at 514 nm and emission wavelengths of 585 and 630 nm. The fluorescence ratio F_{585}/F_{630} was calibrated in separate experiments using cells treated with 10 μM nigericin in Locke's buffer of various pH containing 120 mM KCl. Using the calibration data, intracellular pH was calculated directly from F_{585}/F_{630}. F_{585}/F_{630} was a linear function of pH over pH values between 6.4 and 8.0. In each experiment, to correct for scattered light/autofluorescence, data obtained from cells treated as above but without SNARF-1 incubation were subtracted from data obtained with SNARF-1 incubation.

ZnAF-2F fluorescence

K562 cells attached to poly-D-lysine coated glass coverslips were loaded with ZnAF-2F by incubation for 60 min in Locke's buffer (pH 7.4) at 37 °C containing 5 μM ZnAF-2F

diacetyl ester [21]. The cells were then placed in fresh Locke's buffer and incubated at 37 °C for an additional 30 min. Finally, the cells were placed on ice until used for an experiment. ZnAF-2F fluorescence changes were measured using excitation at 492 nm and emission at 524 nm. Data points were collected at various intervals and saved to a data file. Since ZnAF-2F is not a ratiometric probe, fluorescence data is presented as $\Delta F/F_0$. F_0 is the average fluorescence intensity obtained for each coverslip during a brief preincubation (20–90 s) in Locke's buffer (pH 6 or 8) without added Zn^{2+}. After preincubation, an experimental run was initiated by the addition of various solutions (e.g., Zn^{2+}, CaEDTA, and dH_2O) to the cuvette via a port in the coverslip holder. Opening the door to the cuvette chamber caused a brief disturbance in the recorded data. These data points were deleted and usually amounted to about 2–5 s of data. To calculate $\Delta F/F_0$, F_0 was subtracted from each data point ($=\Delta F$) and was normalized using F_0 ($=\Delta F/F_0$). ZnAF-2F (10 mM in DMSO) was mixed with an equal volume of pluronic acid (20% in DMSO, Molecular Probes) just before use and added with the appropriate dilution in Locke's buffer to obtain the desired final concentration for incubation with cells.

Correction for photodecay

Many experiments using ZnAF-2F required long incubations (up to 1 h), thus a correction for fluorescence changes due to photodecay was necessary. First, we determined the changes in intracellular pH occurring when cells were placed in pH 6 or 8 buffers (intracellular pH dropped from about 7.5 to about 6.7, measured with SNARF-1 fluorescence). The results can be seen in the inset to Fig. 1.

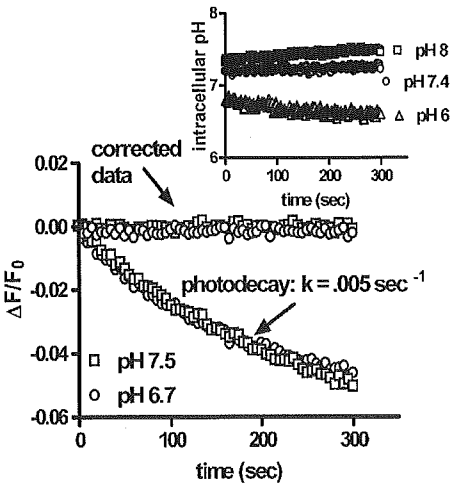

Fig. 1. Analysis of photodecay of ZnAF-2F and the effect of pH. ZnAF-2F free acid (1 μM) was added to 1 μM $ZnCl_2$ (10 mM Hepes) and then fluorescence recorded to observe the photodecay effect. Experiments were performed at either pH 7.5 or 6.7, which were intracellular pH values determined for conditions in this study. For ZnAF-2F results, data are from replicate experiments. Inset: intracellular pH was determined in K562 erythroleukemia cells preincubated with 5 μM SNARF-1 and then placed into either pH 8, 7.4, or 6 Locke's buffer. Intracellular pH was estimated as described in Materials and methods.

Fig. 1 shows that the fluorescence signal decay was fit by a one phase exponential curve. K_{decay} and span were estimated from the decay data (see Fig. 1) using non linear curve fitting (GraphPad Prism ver 4, GraphPad Software, San Diego, CA) to the equation: $y = \text{span} \cdot \exp(-K \cdot x) + \text{plateau}$. $\Delta F/F_0$ values calculated from raw data were corrected at each time point for decay using the equation: fraction remaining $= e^{-K \cdot \text{time}}$. The fraction remaining was subtracted from 1 and multiplied by the span to obtain the correction factor, which was then added to $\Delta F/F_0$ at each time point. The net effect of the correction was to level the fluorescence signal over time (see Fig. 1). No effect of pH was seen on the decay rate. As the decay rate varied slightly from experiment to experiment, each experiment was corrected with its own decay rate.

Results

Previous studies using cultured rat cortical neurons show a robust $^{65}Zn^{2+}$ uptake when cells are placed in buffers containing micromolar concentrations of $^{65}Zn^{2+}$. $^{65}Zn^{2+}$ uptake was inhibited by extracellular acidification and stimulated by intracellular acidification [17–20]. We hypothesized that proton effects are fundamental to the transport mechanism and suggested the mechanism responsible for $^{65}Zn^{2+}$ uptake in cortical neurons could be a Zn^{2+}/H^+ antiporter. In an attempt to identify the protein responsible for pH dependent Zn^{2+} uptake, we took advantage of the well characterized pH dependence of plasma membrane Zn^{2+} transport in cortical neurons to examine the pH dependence of the SLC39A1 protein. The SLC39A1 protein is a logical choice since the kinetic properties of $^{65}Zn^{2+}$ uptake in cortical neurons [17], mirror closely those of the SLC39 family of transporters [4,5]. To test the hypothesis that the SLC39A1 protein (the gene is expressed in the brain) mediates pH dependent $^{65}Zn^{2+}$ uptake, we studied K562 erythroleukemia cells. Importantly, antisense oligonucleotides directed against SLC39A1 expression show nearly complete inhibition of $^{65}Zn^{2+}$ uptake indicating that SLC39A1 expression is sufficient to account for endogenous $^{65}Zn^{2+}$ uptake in K562 cells [5].

The net accumulation of $^{65}Zn^{2+}$ in K562 erythroleukemia cells is inhibited by extracellular acidification

Fig. 2 shows the dependence of the initial velocity of $^{65}Zn^{2+}$ uptake at pH 8 on extracellular Zn^{2+} concentration. The data were fit to a rectangular hyperbola ($y = V_{max} \cdot x)/(K_m + x)$ using GraphPad Prism (ver 4) yielding estimates of 11 μM for the K_m and 0.203 nmol/mg/s for the V_{max}. The inset to Fig. 2 shows that linear uptake is observed at least over the first 20 s at 30 μM extracellular Zn^{2+}added. This is the amount of extracellular Zn^{2+} used in subsequent experiments. However, uptake did not extrapolate to zero uptake at zero time, but to about 0.8 nmol/mg. Zero time uptake was estimated by mixing ice cold cells with ice cold reaction buffer and immediately filtering the mix. The value obtained (0.78 nmol/mg at 30 μM extracellular Zn^{2+}) matched the

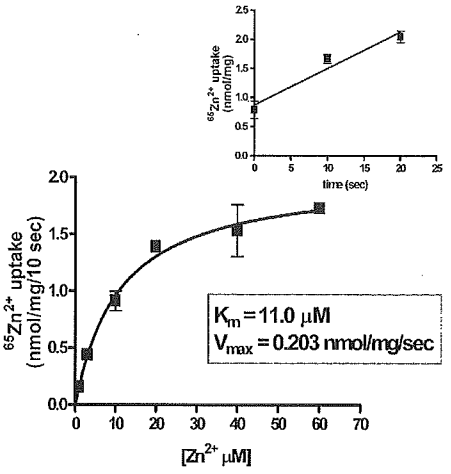

Fig. 2. Concentration dependence of the initial velocity of $^{65}Zn^{2+}$ uptake. K562 erythroleukemia cells were incubated at 37 °C with either 1, 3, 10, 20, 40, or 60 μM $^{65}Zn^{2+}$ added, for 10 s. The reaction was stopped by immediately filtering the cell suspension followed with three washes of ice cold EGTA wash buffer (see Materials and methods). Inset: cells were treated as described above in 30 μM $^{65}Zn^{2+}$ for either 10 or 20 s before stopping the reaction. Zero time was estimated by mixing ice cold cells with ice cold buffer (30 μM $^{65}Zn^{2+}$) and immediately filtering. Each point represents the mean ± SEM of three replicate experiments.

extrapolated zero value, as can be seen in the inset. Zero time $^{65}Zn^{2+}$ uptake most likely represents plasma membrane bound and residual $^{65}Zn^{2+}$ caught on the filters that is resistant to removal by the cold wash buffer. This interpretation was confirmed when comparing $^{65}Zn^{2+}$ uptake data with ZnAF-2F fluorescence changes (see Fig. 4).

Figs. 3A and B show that during its initial phase, total $^{65}Zn^{2+}$ uptake was inhibited as much as 60% by changing the extracellular pH from 8 to 6, an effect similar to that seen in cortical neurons [17]. As a control (see Fig. 3A), it is shown that the inclusion of 1 mM CaEDTA completely inhibits $^{65}Zn^{2+}$ uptake (1 mM CaEDTA is typically used to chelate free extracellular Zn^{2+} because EDTA has a much higher affinity for Zn^{2+} than Ca^{2+}. Thus, free Zn^{2+} is lowered to picomolar levels, whereas free Ca^{2+} is barely affected.). The pH dependence of the initial uptake velocity shows a smooth monophasic curve with an IC_{50} (pH 6.34) estimated from non linear curve fitting (GraphPad Prism ver 4). These data suggest that SLC39A1 protein transport function was inhibited by lowering extracellular pH.

In the presence of elevated extracellular Zn^{2+}, K562 erythroleukemia cells establish a new steady state with elevated free intracellular Zn^{2+}, shown with studies using the cell permeable fluorophore, ZnAF-2F DA, and $^{65}Zn^{2+}$

ZnAF-2F DA is a membrane permeable fluorophore with high affinity for Zn^{2+}, little pH sensitivity, and excellent selectivity over other divalent cations [21]. Fig. 4 shows fluorescence changes observed in K562 cells containing ZnAF-2F after addition of 30 μM Zn^{2+} compared to cells after an equal volume of water was added. When extracellular Zn^{2+} was increased a rising curvilinear trace was obtained, consistent with increasing intracellular free Zn^{2+} (see Fig. 4A). Intracellular free Zn^{2+} appeared to increase gradually until a new steady state was established, approximately 30 min after addition of Zn^{2+}.

As shown above, when K562 cells are placed in Zn^{2+} containing buffers, they accumulate significant amounts of $^{65}Zn^{2+}$ and show detectable ZnAF-2F fluorescence changes because of increased influx, but what is the relationship between these two measurements? Cellular Zn^{2+} content is determined by the relative rates of Zn^{2+} influx and efflux. When Zn^{2+} influx increases one expects an increase in cellular Zn^{2+} content. Conversely, when Zn^{2+} efflux increases, cellular Zn^{2+} content should decrease. When a steady state in free intracellular Zn^{2+} exists, influx and efflux are balanced and total cellular Zn^{2+} remains constant. In studies using ZnAF-2F, fluorescence changes are reporting changes in the free or easily exchangeable pools of intracellular Zn^{2+}. In studies using $^{65}Zn^{2+}$, changes in cellular $^{65}Zn^{2+}$ content can reflect plasma membrane binding, net uptake of $^{65}Zn^{2+}$, and equilibration of radioisotope with nonradioactive Zn^{2+} inside the cell (a reflection of $^{65}Zn^{2+}/Zn^{2+}$ exchange). We have shown that, after placing K562 cells in buffers containing micromolar added Zn^{2+}, influx is immediately increased. A net accumulation of Zn^{2+} occurs

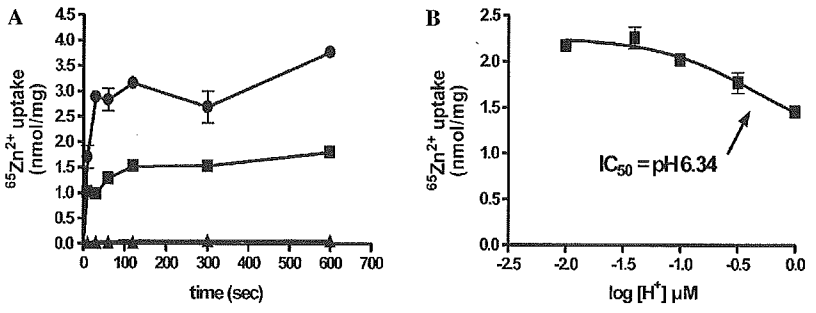

Fig. 3. Effect of pH and Zn^{2+} chelation by EDTA on $^{65}Zn^{2+}$ uptake measured in K562 erythroleukemia cells. (A) K562 erythroleukemia cells were incubated with 30 μM $^{65}Zn^{2+}$ for various times at pH 8 (●), pH 6 (■), or pH 8 containing 1 mM CaEDTA (▲). (B) Uptake reactions were performed in buffer containing 30 μM $^{65}Zn^{2+}$ adjusted to various pH values between 8 and 6. $^{65}Zn^{2+}$ uptake reactions were stopped after 10 s at 37 °C. Data were fit to the equation: y = bottom + (top−bottom)/1 + 10^(x−log IC_{50}) to estimate IC_{50} (GraphPad Prism ver 4). All data points are the means ± SEM of at least three replicate experiments.

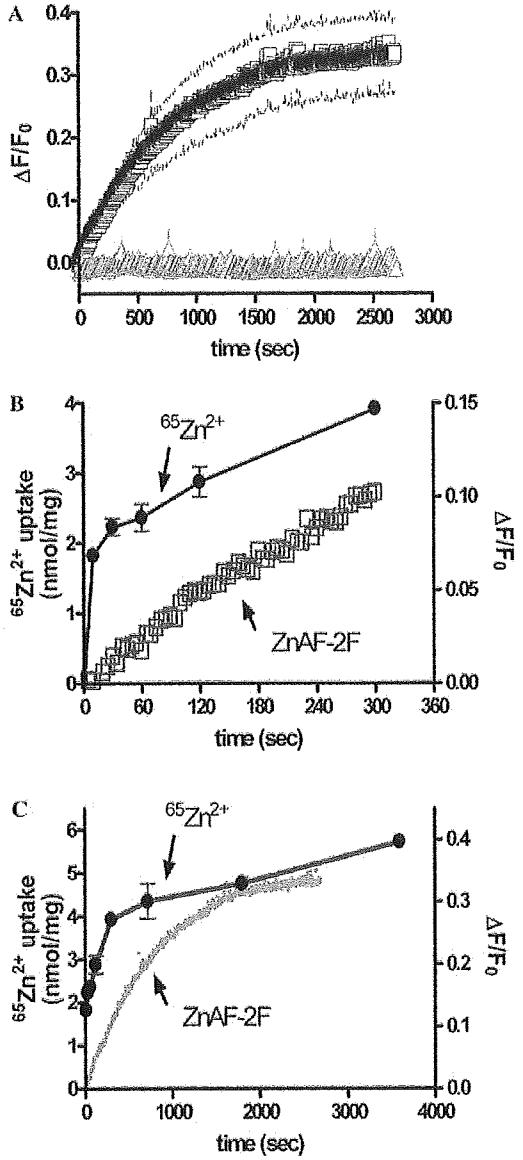

Fig. 4. ZnAF-2F fluorescence changes observed in K562 erythroleukemia cells exposed to increased extracellular Zn^{2+}. K562 erythroleukemia cells attached to glass coverslips were loaded with ZnAF-2F by incubation for 60 min in Locke's buffer (pH 7.4) at 37 °C containing 5 μM ZnAF-2F diacetyl ester. (A) Fluorescence intensity measured after either 30 μM Zn^{2+} (□), or an equal volume of water (△) was added to cells incubating in Locke's buffer pH 8 at 37 °C. Each point represents the means ± SEM (SEM represented as dotted line above and below the data points) of three replicate experiments. (B) Data from (A) (□) are plotted on the same graph with data presented in Fig. 3A—$^{65}Zn^{2+}$ uptake in the presence of 30 μM $^{65}Zn^{2+}$, pH 8 (●). (C) Similar to (B) except data are plotted over a longer time frame (□).

resulting in increasing $^{65}Zn^{2+}$ content and changes in ZnAF-2F fluorescence. Fig. 4B shows that during the initial phase of Zn^{2+} uptake the changes in ZnAF-2F fluorescence and $^{65}Zn^{2+}$ content parallel each other, but differ in that an initial rapid accumulation of $^{65}Zn^{2+}$ is seen. Analysis of initial rates of $^{65}Zn^{2+}$ uptake (Fig. 2) suggests that the initial burst in $^{65}Zn^{2+}$ accumulation is plasma membrane/filter binding. The results of Fig. 4B agree with this interpretation. The transport reaction proceeds until a new steady state is attained (see Fig. 4C), as shown by both ZnAF-2F and $^{65}Zn^{2+}$ data. However, cellular $^{65}Zn^{2+}$ content will slowly continue to increase until the specific activity of $^{65}Zn^{2+}$ inside and outside the cell reaches equilibration, but likely results in little net change in cellular Zn^{2+} content.

The possibility exists that the plateau in ZnAF-2F fluorescence results from saturation or leakage of the dye, not establishment of a new steady state. We wanted to show that the leakage was in fact small and that the robustness of the intracellular dye response was well maintained even after long incubations. To show this, we used a Zn^{2+} ionophore (sodium pyrithione, −50 μM with 30 μM Zn^{2+} added) added either at the start of a reaction or after a steady state had been achieved to maximally load the cells with Zn^{2+}. It can be seen in Fig. 5 that addition of sodium pyrithione results in a large and rapid rise in ZnAF-2F fluorescence when added at the start of the reaction, in response to a large influx of Zn^{2+}. After addition of 30 μM Zn^{2+} alone a new steady state was established, however, addition of sodium pyrithione disturbed this steady state by allowing a rapid influx of additional Zn^{2+}, observed as increased ZnAF-2F fluorescence similar to that seen after addition at the start of the reaction. Thus, the establishment of a new steady state after addition of Zn^{2+}, reflected as a steady level of ZnAF-2F fluorescence, did represent a steady state in intracellular free Zn^{2+} concentration and was not the result of fluorophore saturation or leakage from the cell.

Extracellular acidification inhibits Zn^{2+} influx

In Figs. 6A and B, the effects of extracellular acidification on ZnAF-2F fluorescence changes, with or without Zn^{2+} addition are shown. We saw that the initial rate of

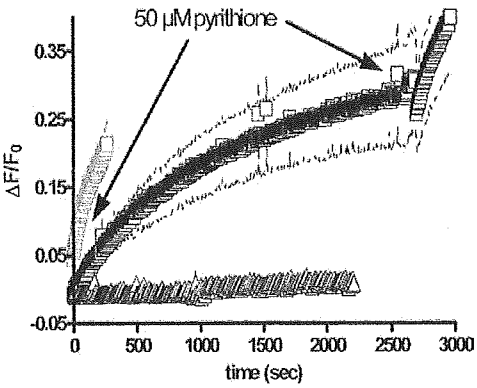

Fig. 5. ZnAF-2F fluorescence changes observed in K562 cells exposed to sodium pyrithione. K562 erythroleukemia cells attached to glass coverslips were prepared as described in the legend to Fig. 4 (30 μM Zn^{2+} added to start the reaction □; or an equal volume of water △). At the indicated times, (see arrows), 50 μM sodium pyrithione was added (pyrithione was not added to the water run). Data are means ± SEM (SEM represented as dotted line above and below the data points) of three replicate experiments.

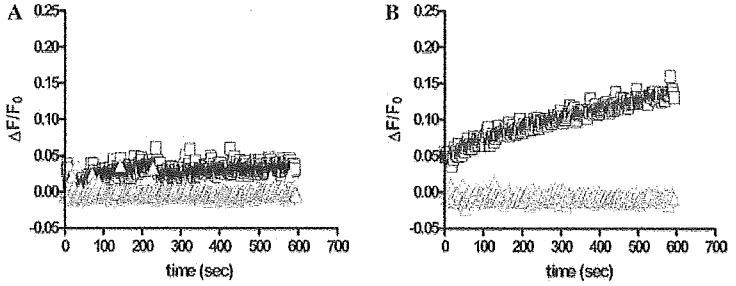

Fig. 6. ZnAF-2F fluorescence changes observed in K562 erythroleukemia cells exposed to extracellular acidification. K562 erythroleukemia cells attached to glass coverslips were prepared as described in the legend to fig. 4. (A) Cells were placed into pH 6 Locke's buffer and at time zero 30 μM Zn^{2+} (□) or an equal volume of water (△) was added. (B) Same as in (A) except that cells were in pH 8 Locke's buffer. All data represent means of at least duplicate experiments.

fluorescence increase observed after addition of 30 μM Zn^{2+} in pH 8 (see Fig. 6B), was almost completely blocked in pH 6 and differed little from that seen in the absence of added Zn^{2+} in either pH 8 or 6 (see Fig. 6A). We conclude that Zn^{2+} influx is inhibited (even in the presence of micromolar added extracellular Zn^{2+}) by extracellular acidification. Since the SLC39A1 protein is the primary, if not only, mediator of Zn^{2+} influx in K562 cells, we must conclude that SLC39A1 transport function is inhibited by extracellular acidification.

Discussion

The findings reported here demonstrate the effectiveness of using ZnAF-2F to monitor changes in intracellular Zn^{2+} and provide consistent evidence that Zn^{2+} influx in K562 erythroleukemia cells was inhibited by extracellular acidification. Our data shows that short term steady state levels of free intracellular Zn^{2+} are largely determined by the relative rates of Zn^{2+} influx and efflux across the plasma membrane. Our data is consistent with distinct pathways for Zn^{2+} influx (SLC39A1 protein mediated) and efflux. We show that under resting conditions, in Locke's buffer, K562 cells maintain a steady state with both Zn^{2+} influx (and presumably efflux) so small as to be undetectable by the methods employed in this study. Zn^{2+} influx is likely small because the contaminating concentration of free Zn^{2+} in Locke's buffer is below the activation level required to stimulate Zn^{2+} influx. Adding micromolar amounts of Zn^{2+} to the Locke's buffer clearly stimulated Zn^{2+} influx. Efflux is small under these conditions because free intracellular Zn^{2+} is small as well.

When Zn^{2+} influx was stimulated, cellular Zn^{2+} rose, and presumably free intracellular Zn^{2+} rose until a new steady state was attained. This study provides evidence that transported $^{65}Zn^{2+}$ readily equilibrated with free intracellular Zn^{2+}. We showed that over relatively short periods of time (up to one hour in this study) free intracellular Zn^{2+} was allowed to increase in response to changes in Zn^{2+} influx. Presumably, under either physiological or pathological conditions, if Zn^{2+} were released from intracellular sequestration sites, a transient rise in free intracellular Zn^{2+} would occur also. Such a rise in free intracellular Zn^{2+} has been shown to occur in neurons after oxidative stress [22,23]. On the other hand, it is thought that long term cellular Zn^{2+} status and presumably free intracellular Zn^{2+} concentrations are regulated by the altered expression of SLC30A1 (Zn^{2+} efflux) and metallothionein [24,25] and the cycling of SLC39 proteins (Zn^{2+} influx) between the *trans*-Golgi network and the plasma membrane [6,26].

But does a free pool of intracellular Zn^{2+} even exist in eukaryotic cells? O'Halloran and co-workers [27,28] make the convincing argument that at least in *Escherichia coli*, metal binding proteins are so effective as to lower free intracellular Zn^{2+} and other metals to femtomolar levels. In eukaryotic cells, glutathione, and free amino acids (e.g., histidine) can act as additional Zn^{2+} binding moieties in addition to metallothionein/thionein pair [29,30]. Although these compounds have low affinity for Zn^{2+}, they exist in millimolar concentrations in the cell and are predicted to lower free intracellular Zn^{2+} to negligible levels. Thus, the Zn^{2+} signal sensed by ZnAF-2F might actually exist as a freely exchangeable (low affinity, bound) pool of Zn^{2+}, such that free Zn^{2+} actually changes little or not at all in our experiments.

This study adds to our growing knowledge of the transport mechanism of SLC39 proteins. SLC39 proteins are responsible for influx and appear to function by facilitated transport, dependent on a concentration gradient to provide the free energy for net movement of Zn^{2+} into the cell. This study provides evidence that SLC39A1 protein transport function is inhibited by extracellular acidification. The pH dependence of SLC39A1 protein transport activity has not been extensively studied [4,5], although the SLC39A2 protein was shown to be activated by bicarbonate ion. We took great care to eliminate bicarbonate effects by using bicarbonate free buffers bubbled with O_2. Thus, we conclude that SLC39A1 protein transport activity is inhibited by extracellular acidification and this effect is not mediated through changes in bicarbonate ion. The IC_{50} of the pH effect is remarkably close to the amino acid histidine ($pK_a = 6.0$), suggesting histidine residues in the protein could play a critical role in the mechanism of pH effects. Sequence analysis of the SLC30 gene family [1] reveals a highly conserved histidine rich domain in the large intracellular loop between

transmembrane domains III and IV (albeit the function of this loop is unclear at present). In addition, transmembrane domains IV–V, which are predicted to be involved in Zn^{2+} translocation, contain histidine residues also. Thus, conserved histidine residues present in SLC39A1 that play a critical role in Zn^{2+} influx may be involved in the pH effect. Finally, it appears likely that the previously reported pH effect on Zn^{2+} transport in cortical neurons [17] is mediated through SLC39A1 protein activity.

Acknowledgments

This work was supported by a grant from the National Institute on Aging and the Provost's Undergraduate Research Fund at OHIO University.

References

[1] D.J. Eide, Pflugers Arch. 447 (2004) 796–800.
[2] L.A. Gaither, D.J. Eide, BioMetals 14 (2001) 251–270.
[3] R.D. Palmiter, L. Huang, Pflugers Arch. 447 (2004) 744–751.
[4] L.A. Gaither, D.J. Eide, J. Biol. Chem. 276 (2001) 22258–22264.
[5] L.A. Gaither, D.J. Eide, J. Biol. Chem. 275 (2000) 5560–5564.
[6] B.E. Kim, F. Wang, J. Dufner-Beattie, G.K. Andrews, D.J. Eide, M.J. Petris, J. Biol. Chem. 279 (2004) 4523–4530.
[7] K. Wang, B. Zhou, Y.M. Kuo, J. Zemansky, J.A Gitschier, Am. J. Hum. Genet. 71 (2002) 66–73.
[8] R.B. Franklin, J. Ma, J. Zou, Z. Guan, B.I. Kukoyi, P. Feng, L.C. Costello, J. Inorg. Biochem. 96 (2003) 435–442.
[9] R.D. Palmiter, S.D. Findley, EMBO J. 14 (1995) 639–649.
[10] A.H. Kim, C.T. Sheline, M. Tian, T. Higashi, R.J. McMahon, R.J. Cousins, D.W. Choi, Brain Res. 886 (2000) 99–107.
[11] L. Huang, C.P. Kirschke, J. Gitschier, J. Biol. Chem. 277 (2002) 26389–26395.
[12] T. Kambe, H. Narita, Y. Yamaguchi-Iwai, J. Hirose, T. Amona, N. Sugiura, R. Sasaki, K. Mori, J. Biol. Chem. 277 (2002) 19049–19055.
[13] S.L. Kelleher, B. Lonnerdal, J. Nutr. 132 (2002) 3280–3285.
[14] C.P. Kirschke, L. Huang, J. Biol. Chem. 278 (2003) 4096–4102.
[15] R.D. Palmiter, T.B. Cole, S.D. Findley, EMBO J. 15 (1996) 1784–1791.
[16] R.D. Palmiter, T.B. Cole, C.J. Quaife, S.D. Findley, Proc. Natl. Acad. Sci. USA 93 (1996) 14934–14939.
[17] R.A. Colvin, Am. J. Physiol. Cell Physiol. 282 (2002) C317–C329.
[18] R.A. Colvin, N. Davis, R.W. Nipper, P.A. Carter, Neurochem. Int. 36 (2000) 539–547.
[19] R.A. Colvin, Neurosci. Lett. 247 (1998) 147–150.
[20] R.V. Balaji, R.A. Colvin, Neurochem. Res. 30 (2005) 171–176.
[21] T. Hirano, K. Kikuchi, Y. Urano, T. Nagano, J. Am. Chem. Soc. 124 (2002) 6555–6562.
[22] E. Aizenman, A.K. Stout, K.A. Hartnett, K.E. Dineley, B. McLaughlin, I.J. Reynolds, J. Neurochem. 75 (2000) 1878–1888.
[23] E. Bossy-Wetzel, M.V. Talantova, W.D. Lee, M.N. Scholzke, A. Harrop, E. Mathews, T. Gotz, J. Han, M.H. Ellisman, G.A. Perkins, S.A. Lipton, Neuron 41 (2004) 351–365.
[24] S.J. Langmade, R. Rauind, P.J. Daniels, G.K. Andrews, J. Biol. Chem. 275 (2000) 34803–34809.
[25] G.K. Andrews, Biochem. Pharmacol. 59 (2000) 95–104.
[26] F. Wang, J. Dufner-Beattie, B.E. Kim, M.J. Petris, G.K. Andrews, D.J. Eide, J. Biol. Chem. 279 (2004) 24631–24639.
[27] L.A. Finney, T.V. O'Halloran, Science 300 (2003) 931–936.
[28] C.E. Outten, T.V. O'Halloran, Science 292 (2001) 2488–2492.
[29] A. Krezel, J. Wojcik, M. Maciejczyk, W. Bal, W. May, Chem. Commun. (Camb.) 6 (2003) 704–705.
[30] W. Maret, J. Nutr. 133 (2003) 1460S–1462S.

Available online at www.sciencedirect.com
SCIENCE DIRECT®
Analytical Biochemistry 350 (2006) 196–201
ANALYTICAL BIOCHEMISTRY
www.elsevier.com/locate/yabio

Detection of oxidative stress-induced mitochondrial DNA damage using fluorescence correlation spectroscopy

Yasutomo Nomura [a,*], Hirobumi Fuchigami [b], Hiroaki Kii [c], Zhonggang Feng [b], Takao Nakamura [a], Masataka Kinjo [c]

[a] *Department of Environmental Life Science, Graduate School of Medical Science, Yamagata University, Yonezawa, Yamagata 992-8510, Japan*
[b] *Department of Bio-System Engineering, Faculty of Engineering, Yamagata University, Yonezawa, Yamagata 992-8510, Japan*
[c] *Laboratory of Supramolecular Biophysics, Research Institute for Electronic Science, Hokkaido University, Sapporo 060-0812, Japan*

Received 5 September 2005
Available online 25 January 2006

Abstract

Using fluorescence correlation spectroscopy (FCS), we tested the feasibility of rapid detection of oxidative damage of mitochondrial DNA (mtDNA) in a small volume. The complete mtDNA genome was amplified by long polymerase chain reaction (LPCR), and the product was fluorescently labeled with an intercalating dye, YOYO-1. The fluorescence autocorrelation function was analyzed using a simple two-component model with the diffusion time of 0.21 ms for the LPCR primer and 18 ms for the mtDNA LPCR product. When human embryonic kidney 293 (HEK-293) cells were exposed to 0.4 mM H_2O_2, the fraction of the mtDNA LPCR product decreased significantly. In contrast, the fraction of the nuclear-encoded β-globin LPCR product remained unchanged. The analysis time of FCS measurement was very short (5 min) compared with that of gel electrophoresis (3 h). Thus, FCS allowed the rapid detection of the vulnerability of mtDNA to oxidative stress within a small volume element at the subfemtoliter level in solution. These results suggest that the LPCR–FCS method can be used for epidemiological studies of diseases caused by mtDNA damage.

Keywords: Fluorescence correlation spectroscopy; Long PCR; Mitochondria; Oxidative stress

Damaged mitochondrial DNA (mtDNA)[1] has been reported to be involved in a variety of human diseases, including diabetes, cancer, Parkinson's disease, and Alzheimer's disease [1,2]. However, the factors responsible for the damage in the diseases remain to be determined. Major candidates for the primary source of damage may be reactive oxygen species (ROS). Mitochondria produce ROS during normal respiration but can metabolize them only partially. Despite the defense system, mtDNA is particularly vulnerable because it is partially associated with the inner mitochondrial membrane [3,4].

So far, damage in mtDNA has been detected by some common methods such as Southern blotting [5] and HPLC–electrochemical detection [6]. However, one disadvantage of these techniques is that they require large quantities of mtDNA and nuclear DNA. Furthermore, because of the cost of sample preparations and the long analysis time of several hours, the techniques might not be suitable for a large-scale epidemiological study of mtDNA damage caused by oxidative stress.

To overcome these disadvantages, we propose a new methodology combining fluorescence correlation spectroscopy (FCS) with long polymerase chain reaction (LPCR). The LPCR used in the current study quantitatively amplifies the entire intact mtDNA genome alone in a small sample [7]. This technique is based on the premise that DNA

* Corresponding author. Fax: +81 238 26 3357.
E-mail address: ynomura@yz.yamagata-u.ac.jp (Y. Nomura).

[1] *Abbreviations used:* mtDNA, mitochondrial DNA; ROS, reactive oxygen species; FCS, fluorescence correlation spectroscopy; LPCR, long polymerase chain reaction; HEK-293, human embryonic kidney 293; DMEM, Dulbecco's modified Eagle's medium; PBS, phosphate-buffered saline.

0003-2697/$ - see front matter © 2006 Elsevier Inc. All rights reserved.
doi:10.1016/j.ab.2006.01.010